

1 Near-surface characterization and delineation of water 2 preferential flow-pathways at South Deep Gold Mine, South 3 Africa

4 Sikelela Gomo¹, Farbod Khosro Anjom², Chiara Colombero², Mohammadkarim Karimpour², Bibi
5 Ayesha Jogee¹, Musa S.D. Manzi¹, Laura V. Socco^{2,3}

6 ¹School of Geosciences, University of the Witwatersrand, Johannesburg, Private Bag, Wits, 2050, Republic of South
7 Africa.

8 ²Department of Environment, Land and Infrastructure Engineering, Politecnico di Torino, Turin, 10129, Italy.

9 ³Department of Geoscience and Engineering, Delft University of Technology, Delft.

10 *Correspondence to:* Sikelela Gomo (1488846@students.wits.ac.za)

11 **Abstract.** Velocity models of the shallow subsurface (a few hundred ~~of~~ meters) are important in near-surface
12 characterization, improving seismic mapping resolution at depth, and constraining deeper geological models. It is
13 therefore interesting to retrieve them from deep seismic exploration data. We compute the near-surface shear wave
14 velocity model in the vicinity of South Deep Gold Mine, using surface waves present in the small-offset 2D and 3D
15 seismic reflection data acquired between 2022 and 2023 at the mine for research, mine planning, and development
16 purposes. The obtained near-surface model is then used to (1) characterize the near-surface, and (2) better constrain
17 the interpretation of possible water preferential flow-pathways (faults, fracture zones, and dykes) mapped at mining
18 levels, that enable the migration of water from overlying aquifer systems (< 0.5 km depth) to the mining levels (~ 3
19 km depth). The analysis is carried-out on reflection seismic data acquired for deep mineral exploration, where the
20 acquisition parameters were not optimized for surface wave techniques and the reciprocity principle is used to improve
21 the data density, coverage, and near-surface mapping resolution. The lithostructural information retrieved from the
22 produced pseudo-2D and 3D shear wave velocity models is consistent with information obtained from available
23 surface borehole data and published records in the study area. To investigate the structural linkage between the deep
24 mining levels and shallow groundwater aquifers, we integrated the near-surface shear wave velocity model produced
25 from the small-offset 2D and 3D reflection seismic data with the large-offset 2003 3D reflection seismic data, and
26 geological structures derived from underground mapping, and exploration drilling. The shear wave velocity models
27 help define the faults, fractures, and dykes that compartmentalize the near-surface groundwater aquifer systems. The
28 large-offset legacy 2003 3D seismic data, underground mapping, and exploration drilling provide a better definition
29 of the orebody and its offsets (e.g., faults) at the mining level. The integrated data show that several geological
30 structures (e.g., faults and dykes), defined by legacy seismic data, underground drilling, and mapping, cross-cut the
31 mining levels at ~ 3 km depth and intersect the near-surface aquifers, thus making these structures possible preferential
32 flow-pathways for water migration to the deep mining levels. The results of the interpretation illustrate the advantages
33 of integrating shallow and deep subsurface information to constrain the timing of geological events and mitigate the

34 risks associated with water ingress to the mining levels. The final model produced can be used for future mine
35 development, improving safety and production, and for the extension of the Life of Mine (LoM).

36

37 **1 Introduction**

38 The Mesoarchean-aged Witwatersrand Basin hosts the largest known gold deposit in the world and has produced more
39 gold than any other ore province globally (Frimmel, 2019). Seismic techniques have been used extensively in the
40 exploration of the Witwatersrand Basin, mainly for mapping and evaluating gold-bearing quartz pebble conglomerates
41 (locally termed ‘reefs’) for mining purposes (i.e., planning, production, and risk mitigation) and for imaging faults
42 and dykes. Seismic imaging of faults and dykes, in particular, is important in deep underground gold mines as these
43 structures might (1) act as possible preferential flow-pathways for water and methane migration into the mining levels,
44 (2) cross-cut the orebody and make it impractical to mine (Campbell and Crotty, 1988; Pretorius et al., 1989; Gibson,
45 2005; Manzi et al., 2012a), and (3) cause damaging seismic events (Masethe et al., 2023). The first 3D application of
46 seismic techniques in hard-rock mining environments, particularly for mineral exploration, trace back to the surveys
47 conducted by Campbell and Cotty (1988, 1990) at South Deep Gold Mine in 1986 in the Witwatersrand Basin.
48 Campbell and Crotty (1990) applied active-source surface 3D seismic surveys to image the gold-bearing horizons and
49 geological structures at depths down to 3.5 km below ground surface. This pilot study investigated and demonstrated
50 the potential that the 3D seismic technique has in hard-rock environment for mineral exploration. In 2003, Gold Fields
51 commissioned one of the largest 3D seismic surveys in the Witwatersrand basin to map the deep-seated gold deposits
52 (e.g., Ventersdorp Contact Reef, VCR) and subsurface geological structures (e.g., faults and dykes) across its Kloof
53 and South Deep gold mines for mine planning purposes (Manzi et al., 2012a). The legacy 2003 Kloof-South Deep
54 Gold Mine data have been the subject of several studies over the past 20 years, given the size of the survey area and
55 the unique nature of the data, particularly the strong seismic reflections associated with deep-seated gold-bearing
56 horizons and the delineation of complex geological structures that cross-cut the gold deposits (Manzi et al., 2012a,b;
57 Manzi et al., 2013a,b). The data have also been used by Manzi et al. (2012b) to map potential conduits of water and
58 methane at deep mining levels of the Kloof Gold Mine. They have been used to constrain Neoproterozoic tectonic history
59 and the ore genetic models in the Witwatersrand basin (Manzi et al., 2013b; Malehmir et al., 2014).

60 Between 2022 and 2023, high-resolution 2D and 3D deep seismic reflection (DSR) surveys were conducted at South
61 Deep Gold Mine as part of the ERA-MIN3 Future project (Rapetsoa et al., 2025). The work mainly focused on testing
62 the modern seismic technologies to image the deep (~ 3 km) gold-bearing horizons such as the Ventersdorp Contact
63 Reef (VCR), Upper Elsburg Reefs (UER), and complex geological structures (e.g., faults and dykes) that cross-cut the
64 orebodies. The seismic surveys used a seismic nodal system incorporating one vertical and three component recorders
65 connected to 5 Hz geophones, broadband micro-electromechanical system (MEMS) accelerometers, distributed
66 acoustic sensing technology, and a 6-ton broadband (2-200 Hz) seismic vibrator operating with sweep lengths between
67 24s and 48s (Rapetsoa et al., 2025). In this work, we utilize the surface waves (SWs) present in the DSR survey data
68 acquired at the mine to estimate the near-surface shear-wave (S-wave) velocity model [inat](#) the vicinity of the mine,
69 which is used to better understand the near-surface stratigraphic (lithological) and structural (e.g., faults and dykes)

70 geological variations in the study area. We then integrate the near-surface S-wave velocity model with the 2003 legacy
71 seismic data and mine geological structures to investigate the structural linkage between shallow geology (aquifers)
72 and deep mining levels, where the orebody is located, to constrain the timing of structural activities and determine
73 potential preferential flow-pathways for water ingress into the mining levels.

74 The near-surface is a geologically complex environment, often consisting of heterogeneous structures characterized
75 by highly weathered and diverse materials, i.e., that may vary from loose, fractured, to solid rocks, which have the
76 potential to significantly obscure the ability to resolve deeper lying seismic targets (Sheriff, 2002; Zhou et al., 2010;
77 Strong, 2018). Near-surface characterization is an essential process in exploration, mining, engineering, and
78 environmental studies as it can provide information that can be used to improve the imaging of deeper lying geological
79 structures, conducting risk assessments, efficiently plan projects, planning, and for designing and constructing safer
80 and better-performing mining, environmental, and civil engineering infrastructures (Laake et al., 2008; Zhu et al.,
81 2008; Socco et al., 2010; Pegah and Liu, 2016; Papadopoulou et al., 2020). The application of seismic surface wave
82 (SW) analysis to determine near-surface velocity models at hard-rock sites is limited due to the challenge of obtaining
83 good-quality data (Socco et al., 2019; Papadopoulou et al., 2020; Wilczynski et al., 2025). The quality of SW data at
84 hard-rock mining sites can be severely affected by (1) the presence of lateral heterogeneities (e.g., dykes, fractures,
85 and faults) which can generate scattering and back reflections (Pileggi et al., 2011; Malehmir et al., 2015); (2) noise
86 generated by mining activity (e.g., blasting, excavations, drilling, crushing, moving heavy machinery, and mining
87 operations) (Urosevic et al., 2007; Graczyk et al., 2015); and (3) variable and extreme near-surface conditions caused
88 by the presence of hard and rugged topography, roads, areas of outcropping hard rocks, and the presence of swampy
89 soils or dense vegetation (Saunders et al., 1991; Eaton et al., 2003; Heinonen et al., 2011; Malehmir et al., 2017).
90 However, the dominance of SWs in seismic records, their high sensitivity to near-surface properties, their ability to
91 resolve low-velocity zones or soft layers bounded by high-velocity materials, and their ability to avoid the water-
92 masking effect in saturated media, make them a powerful tool for near-surface imaging (Foti et al., 2002; Socco and
93 Strobbia, 2004).

94 This paper presents the application, potential, and benefits of conducting SW analysis to reflection seismic data mainly
95 acquired for deep targeting in a mining environment. Multichannel analysis of surface wave (MASW) and the
96 Laterally Constrained Inversion (LCI) are applied to high-resolution 2D and 3D seismic data to estimate the near-
97 surface S-wave velocity model within the top ~ 300 m in the vicinity of South Deep Gold Mine. Since the deep
98 exploration data acquired at the mine are not optimized for SW analysis (i.e., characterized by coarse spatial sampling)
99 and are therefore not ideal for SW analysis, we utilize the reciprocity theorem to extract all the possible information
100 in the data, and increase the data coverage by providing a grid of orthogonal sets of dispersion curves along receiver
101 and source lines. Comparison with available borehole data in the vicinity of the mine indicates that the conducted
102 analysis is sensitive to stratigraphic and structural variations beneath the acquired DSR surveys and resolves them
103 quite well with depth. Lastly, we integrate the obtained near-surface S-wave velocity model with existing and available
104 legacy 2003 active-source P-wave seismic reflection data, mine mapping, and drilling information to investigate the
105 structural continuity and connectivity between the shallow aquifers (< 0.5 km) and deep mining levels (~ 3 km). These

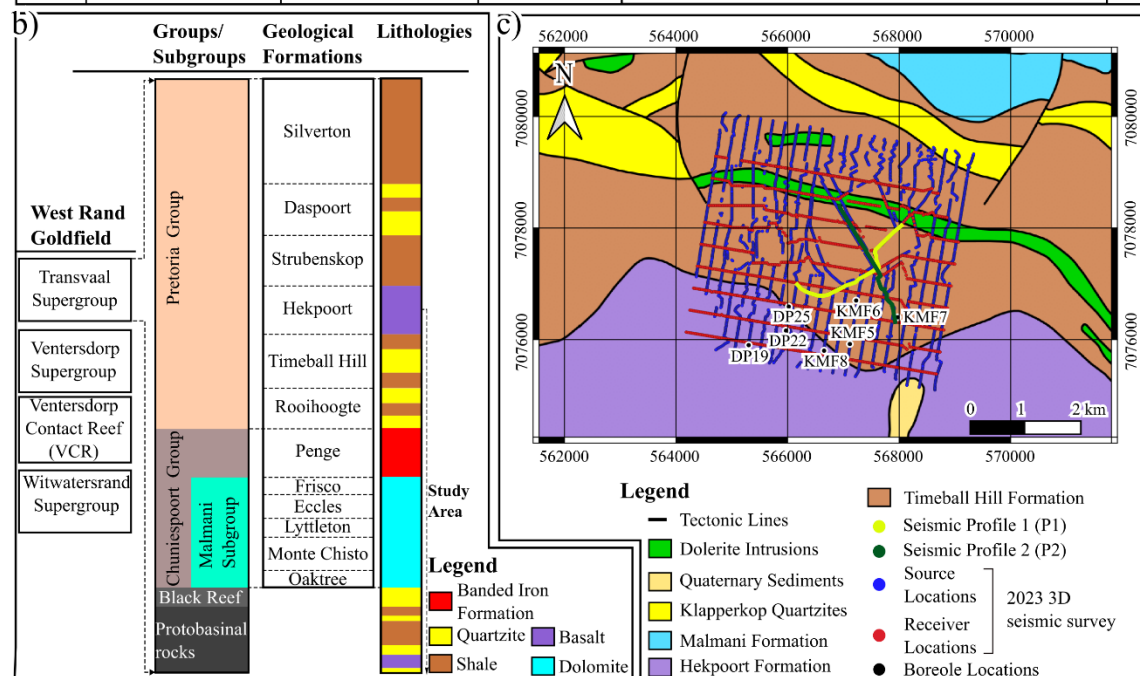
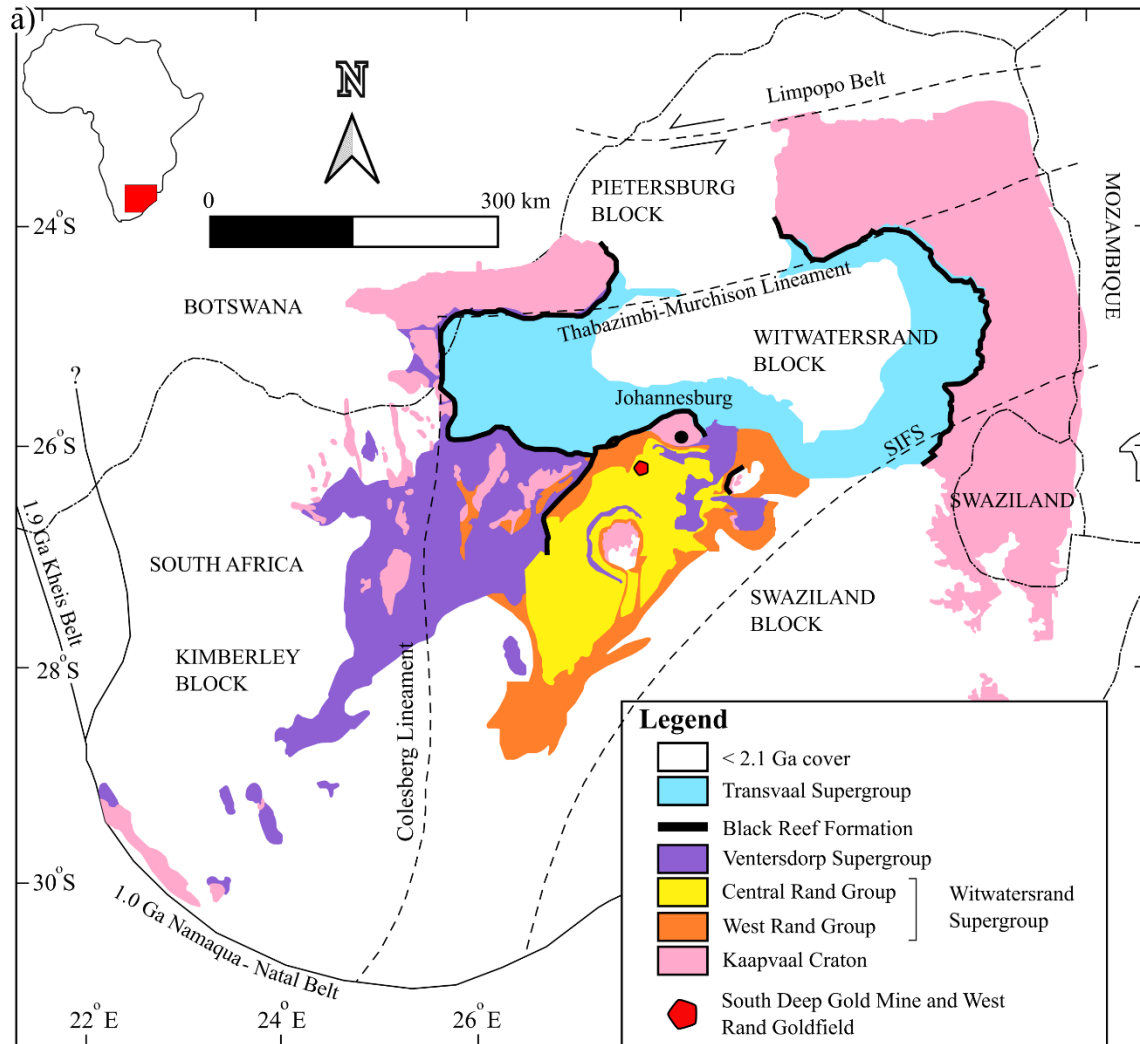
106 mine-mapped structures are well known in the Witwatersrand gold mines (e.g., South Deep Gold Mine and Kloof
107 Gold Mine) to be associated with mining-induced seismicity, water migration, and methane gas pockets (Manzi et al.,
108 2012b; Masethe et al., 2023). The existing large-offset legacy 2003 3D seismic data provides high-resolution imaging
109 of subsurface geological structures from 0.5 km up to 6 km below the ground surface. The integration of the near-
110 surface S-wave model with the large-offset legacy 3D seismic data, underground mapping, and drilling information
111 enabled the tracking (vertically) of these structures through the thick 3 km strata from their known positions at the
112 mining levels to the near-surface. Thus, these different methods and datasets were integrated to overcome their
113 inherent limitations and leverage their strengths.

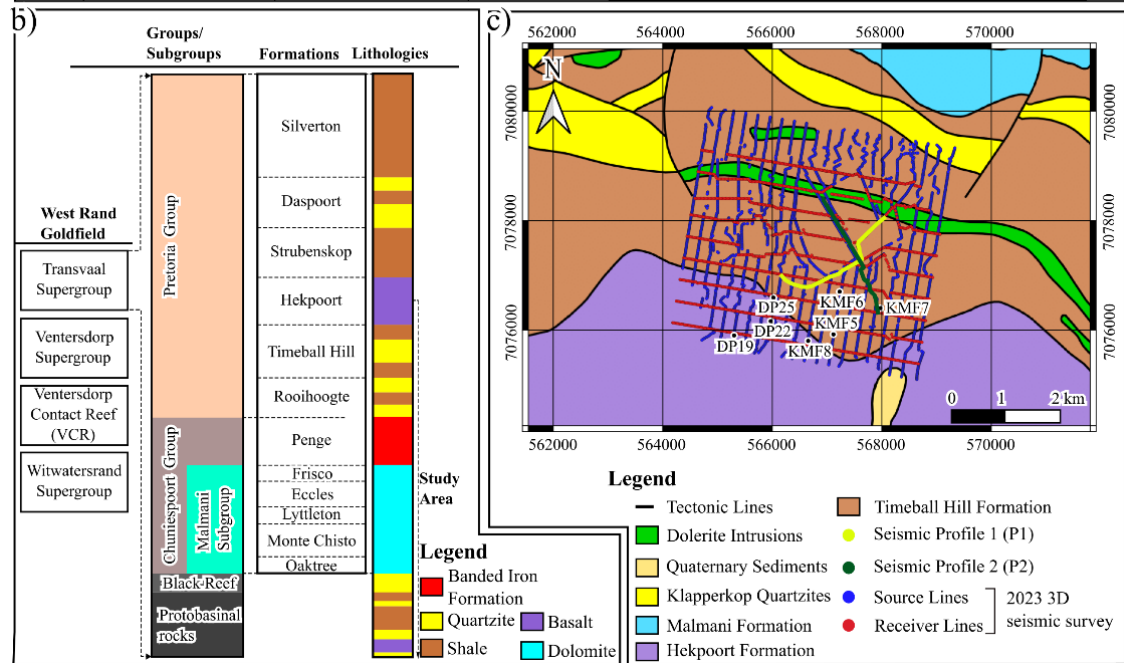
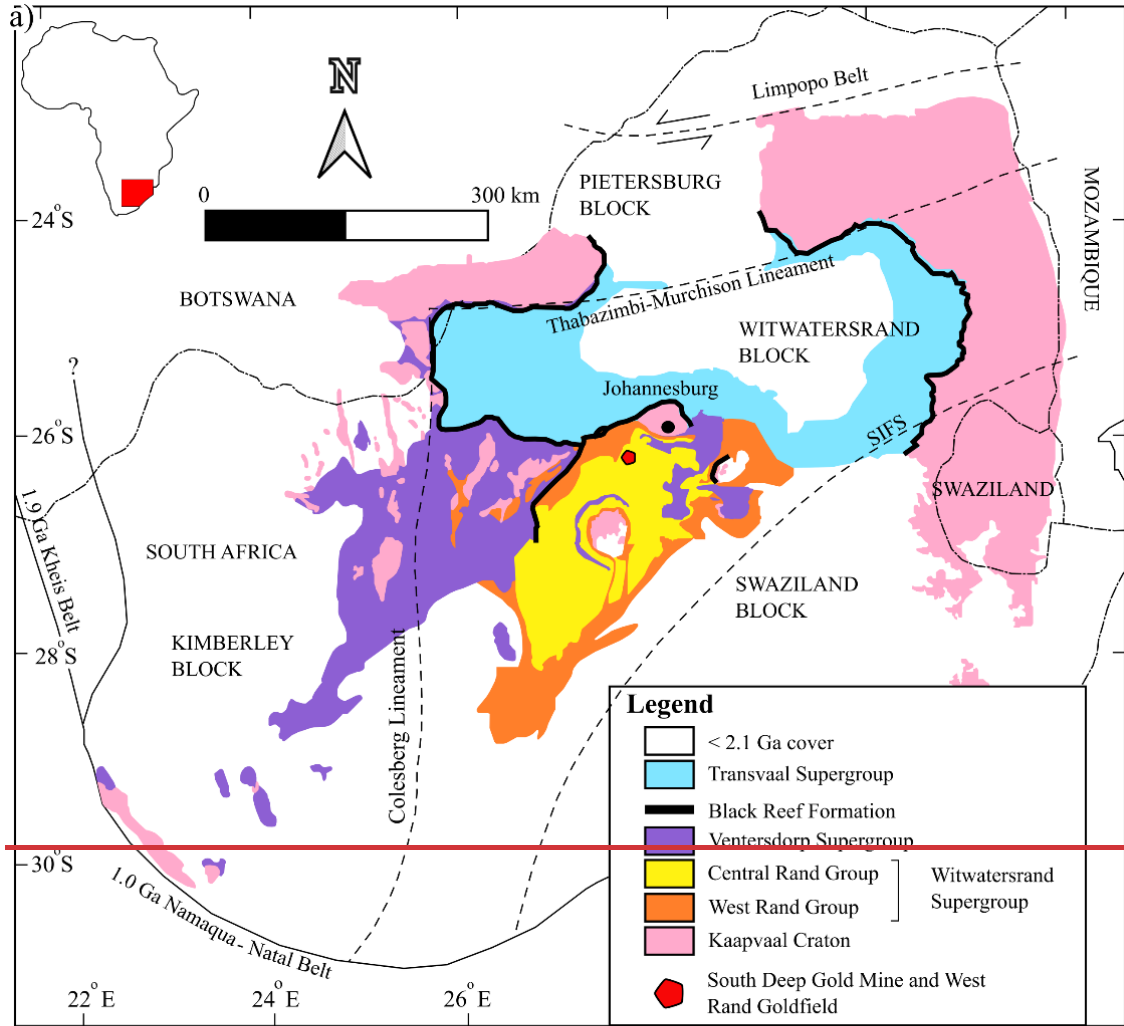
114 In this paper, we (1) describe the mining site and its geological setting, (2) present the seismic data acquisition
115 parameters and the characteristics of the data, and outline the processing and inversion strategy, and (3) discuss the
116 obtained velocity models in connection with surface borehole data, underground mine-mapped structures, and legacy
117 deep seismic data.

118

119 **2 Site and data**

120 South Deep Gold Mine is situated southwest of the city of Johannesburg, in the southern portion of the West Rand
121 Goldfield and on the northern margin of the Witwatersrand Basin (Fig. 1a). Excluding the Archaean granite-greenstone
122 terrains (basement rocks) of the Kaapvaal Craton and basaltic-rhyolitic lavas ~~volcanic~~—and siliciclastic
123 metasedimentary unit of the Dominion Group ~~sedimentary rocks of the Dominion Group~~ that underly the rocks of the
124 Witwatersrand Supergroup, constituting the general setting in the West Rand Goldfield are the rocks of the, from
125 oldest to youngest, Witwatersrand, Ventersdorp, and Transvaal Supergroups (Kositsin and Krape, 2004). The rocks
126 of the Ventersdorp Supergroup are unconformably overlain by the Black Reef quartzite formation of the Chuniespoort
127 Group belonging to the late Archean to early Proterozoic Transvaal Supergroup (Fig. 1b; Martin et al., 1998). The
128 Transvaal Supergroup is a thick succession of chemical and sedimentary rocks, hosting well-preserved volcanic and
129 glaciogenic units (Eriksson et al., 1993b; Bekker et al., 2014;) and world-class iron (Fe) and manganese (Mn) ores
130 (Bekker et al., 2014; Smith and Beukes, 2016; Franchi, 2018) and comprises of the lower Chuniespoort and upper
131 Pretoria Groups (Martin et al., 1998). The Chuniespoort Group dolomites consist of karst systems rich in water, which
132 is primarily responsible for water inflow and inrush into mine shafts and mining levels (Van Niekerk and Van Der
133 Walt, 2006).



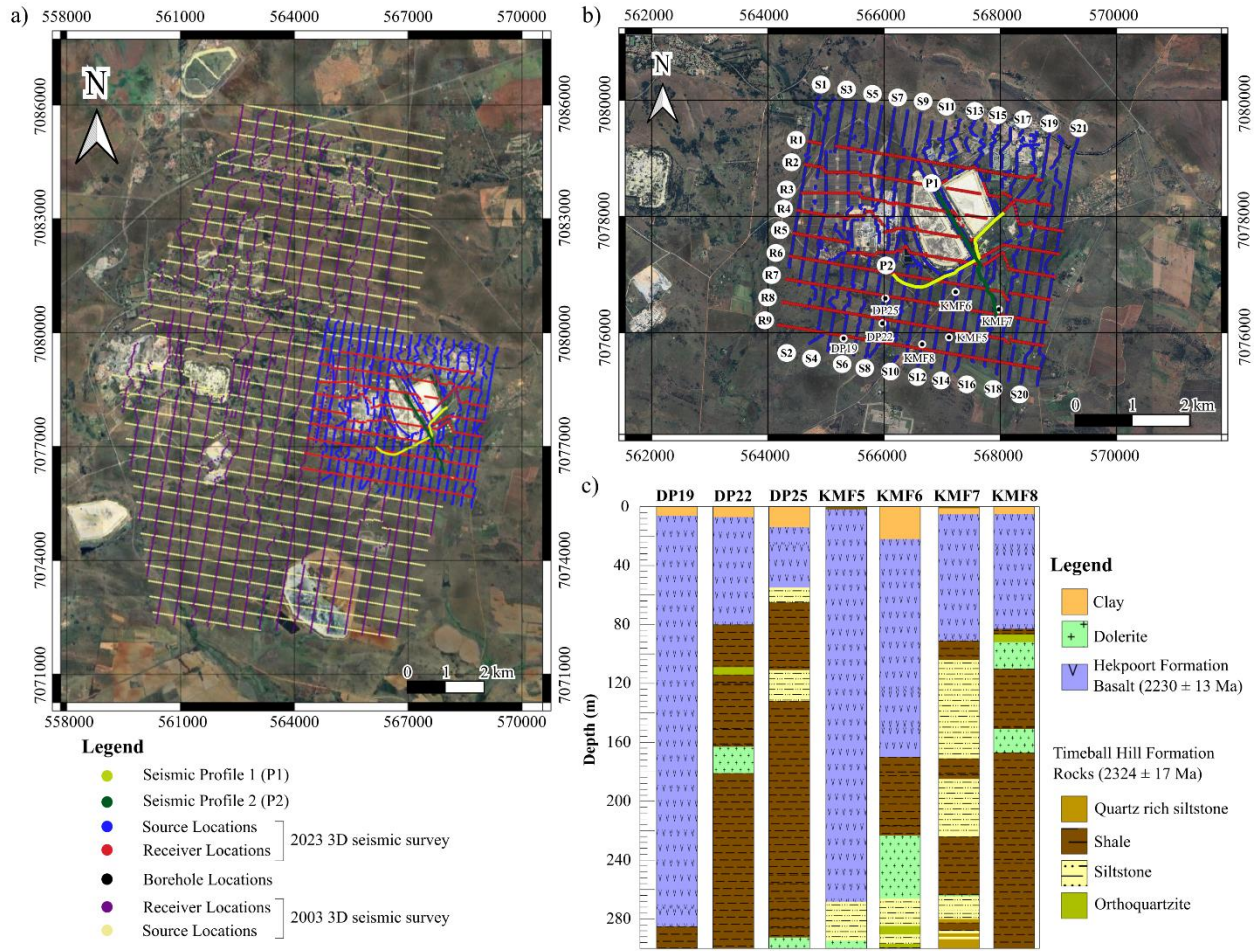


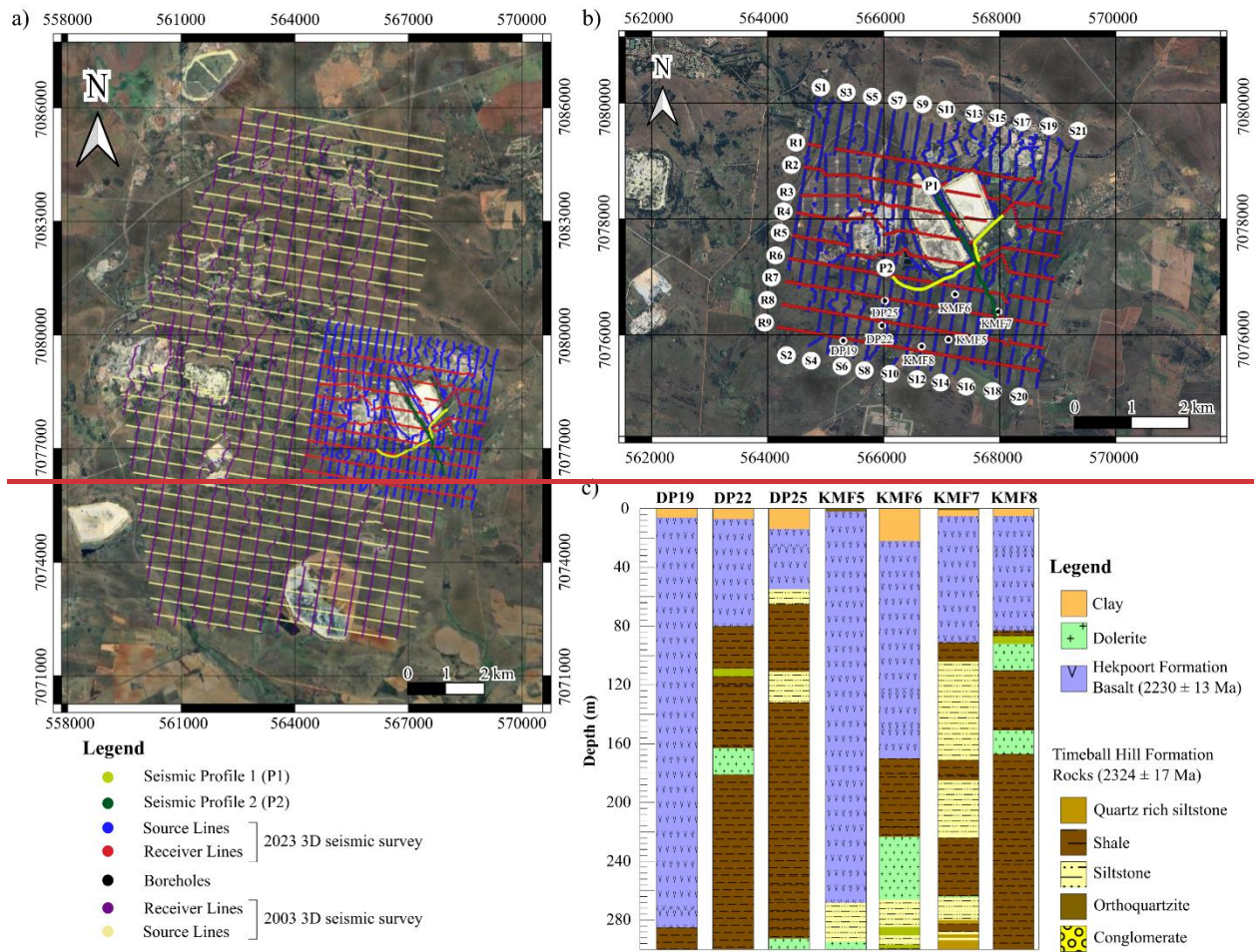
136 **Figure 1: (a) Simplified geological map showing both surface and subsurface distribution of the main Archaean**
137 **stratigraphic units of the Kaapvaal Craton. The map shows the distributions of the Witwatersrand (comprised of the West**
138 **Rand and Central Rand Groups), Ventersdorp, and the Transvaal Supergroups (modified after Frimmel, 2014). (b)**
139 **Generalized stratigraphic column of the uppermost rocks in the Transvaal Supergroup, indicating the uppermost rock**
140 **units outcropping in the study area. (c) A simplified geological map of the study area showing the locations of the high-**
141 **resolution 2D profiles (P1- dark green and P2-yellow), and the receiver (red) and source (dark blue) lines of the 2023 3D**
142 **seismic survey acquired in the vicinity of the mine. The map is plotted using the WGS 1984 UTM Zone 35S coordinate**
143 **system. SIFS is the Saddleback-Inyoka Fault System.**

144

145 Predominantly outcropping in the vicinity of South Deep Gold Mine are the rocks of the Pretoria Group (2350 Ma-
146 2250 Ma; Walraven et al., 1990; Martin et al., 1998). The Pretoria Group forms the upper part of the Transvaal
147 Supergroup and primarily consists of a succession of shales, quartzose and arkosic sandstones, and significantly
148 interbedded basaltic-andesitic volcanic rocks, and subordinate conglomerates, diamictites, and carbonate rocks
149 (Killick, 1992; McCarthy, 2006). In the northern portion of the South Deep Gold Mine, rocks of the Malmani
150 Subgroup, Timeball Hill Formation, and Klapperkop Quartzites are present, while south of the mine, outcrops of
151 basaltic lava and tuff of the Hekpoort Formation exist (Fig. 1c; Osburn et al., 2014). Figure 2a and b show the locations
152 of the legacy, large-offset 2003 and 2022-2023 2D and 3D seismic surveys. In Figure 2c, we show the borehole logs
153 drilled in proximity to the 2D and 3D seismic surveys acquired in the study area between 2022 and 2023 (see Figures
154 1c and 2b for borehole location). The logs include the lithological variation within the top 300 m of the study area and
155 are later used to constrain the conducted SW analysis interpretation. The borehole logs illustrate that, south of the
156 mine, the 2230 ± 13 Ma (Burger and Coertze, 1973) Hekpoort Formation basalts constitute the uppermost rocks and
157 are underlain by the 2324 ± 17 Ma (Dorland, 2004) metasedimentary rocks of the Timeball Hill Formation (Fig. 2c).
158 Tectonically, the Transvaal Supergroup is structurally complex and has undergone several episodes of deformation
159 (Veevers, 1981; Vermaak et al., 1994; Coward et al., 1995; Manzi et al., 2013a,b; Nwaila et al., 2022). In particular,
160 the rocks of the Pretoria Group are displaced by post-Pretoria Group extensional and thrust faults that displace both
161 the Pretoria Group rocks and the base of the Transvaal Supergroup (Cousins, 1962). The post-Pretoria Group tectonic
162 events likely led to the reactivation of pre-Transvaal Supergroup faults, which are imaged in the 2003 legacy 3D
163 seismic data and confirmed by underground drilling and mapping (Manzi et al., 2013a,b; Nwaila et al., 2020a).
164 Movement along faults inevitably resulted in the creation of numerous fracture systems, which can be observed
165 underground (if exposed). The study area is also characterised by numerous sills and dykes that intruded at different
166 geological ages and have been subjected to several investigations. The sills and dykes are of various ages, such as
167 known post-Karoo dykes of pre-Cretaceous and Cretaceous age (145 - 66 Ma), Karoo (150 Ma), Pilanesberg (1.30
168 Ga), Vredefort meteorite impact event (2.05 Ga), the Bushveld Igneous Complex magmatism (2.03 Ga), Transvaal
169 (2.20 Ga), and Ventersdorp (2.60 Ga) (Frimmel, 2014; Frimmel and Nwaila, 2020). Current mining activities can also
170 reactivate faults and dykes, causing large seismic events, and promoting water infiltration, movement, and circulation
171 (Masethe et al., 2023). The intersection of water conduits during mining often negatively affects the productivity of

172 the mine and increases the safety risk to mine personnel and infrastructure. Thus, their delineation is important in
173 ensuring mine safety, longevity, and increased productivity.





175
 176 **Figure 2: a) Satellite map showing the legacy 2003 3D Kloof-South Deep and the 2022-2023 3D South Deep Gold Mine**
 177 **seismic surveys. (b) Zoomed in satellite map of the 2023 South Deep seismic survey. Both satellite maps are plotted using**
 178 **the WGS 1984 UTM Zone 35S coordinate system. (c) Representative borehole logs located within the study area and**
 179 **showing the dominant rock types of the top 300 m.**

180

181 **3 Methodology**

182 **3.1 Seismic data acquisition**

183 Active-source surface 2D and 3D seismic data were acquired between 2022 and 2023 within the framework of the
 184 ERA-MIN3 Future Project, aimed at imaging the subsurface geology and the orebody at South Deep Gold Mine. The
 185 acquired two 2D high-resolution seismic lines (P1 and P2, Figs. 1c and 2a, b) were positioned such that they traversed
 186 the surface zone directly above the mine tunnels, located at a depth of ~3.5 km. The 3D seismic survey covers a wider
 187 area of approximately 4.4 km by 4.7 km, with the mine tunnels located at the centre of the survey area. The acquisition
 188 parameters are summarized in Table 1. The 2D profiles were acquired using a 6-ton seismic vibrator (mini-vibe)
 189 employing a linear sweep of 24 s and a sweep frequency ranging from 2-200 Hz. P1 is north-south orientated and has

190 a profile length of 2420 m, while P2 is east-west orientated and has a profile length of 2650 m. The two profiles were
 191 acquired using 243 and 266 wireless remote acquisition units spaced 10 m apart and connected to 5 Hz vertical
 192 component geophones, respectively. Two sweeps were generated at every receiver and every second receiver location
 193 for P1 and P2, respectively.

194 The 3D seismic survey was acquired using two broadband mini-vibes employing a slip-sweep acquisition technique
 195 with a slleep time of 30 s, a single linear sweep of 48 s, and a frequency ranging from 4 to 150 Hz. The grid consisted
 196 of 9 receiver lines (north-south orientated and 400 m apart), with a receiver spacing of 25 m, and 21 source lines (east-
 197 west orientated and 225 m apart), and with a source spacing increment of 12.5 m, forming an orthogonal acquisition
 198 patch. The data were recorded using a total of 1605 wireless remote acquisition units connected to 5 Hz vertical
 199 component geophones and consisted of 3725 shot points.

200 The units used to record both the 2D and 3D surveys were programmed to switch on at 8:00 am and off at 17:00 pm,
 201 South African time, during which the seismic data were recorded in continuous mode, at a 2 ms sampling rate. After
 202 the completion of the survey acquisition stage, all the separate sweeps were later isolated and 6 s of the records were
 203 extracted from the recording units using the GPS time tagged for each sweep. The layouts of the surveys, however,
 204 were distorted by natural (river and swamps) and man-made features (mining infrastructure, two large tailings dams,
 205 roads, and nearby settlements) present in the vicinity of the mine, thus, sharp turns and gaps were introduced in the
 206 data (crooked profiles; Figs. 1c and 2b). The study area is characterized by a significant but gentle E-W elevation
 207 variation of approximately 100 m in the southern portion, a gentle 10 m E-W elevation variation in the northern
 208 section, and a 20 m N-S elevation variation in the middle section of the study area. Throughout the study area, the
 209 bedrock is largely covered by residual soil. The 2023 South Deep Gold Mine seismic survey was designed to overlap
 210 with the 2003 Kloof-South Deep survey, which was designed to image the deep-seated Ventersdorp Contact (VCR)
 211 orebody and major geological structures to assist with mine planning and development (Fig. 2a, Manzi et al., 2012a).
 212 The acquisition parameters and processing sequence of the 2003 3D seismic survey are summarized by Manzi et al.,
 213 (2012a,b). In summary, the survey was acquired using 4 vibroseis trucks (sweep: linear, 16s, 12-96 Hz) over an area
 214 of approximately 96 km² with the receiver spacing of 50 m, receiver line spacing of 400 m, shot spacing of 50 m, and
 215 shot line spacing of 450 m.

216 **Table 1:** Acquisition parameters of the 2D and 3D surveys conducted at South Deep Gold Mine [in 2022-23](#).

Survey Parameters	Profile 1 (P1)	Profile 2 (P2)	3D Survey
Profile length	2420 m	2650 m	4.5 x 4.7 km
Profile type	-	-	Slip-sweep, <u>sl</u> leep time: 30 s
Sampling rate	2 ms	2 ms	2 ms
Sweep length	24 s	24 s	48 s
Sweep frequencies	2-200 Hz (linear sweep)	2-200 Hz (linear sweep)	4-150 Hz (custom sweep)
Receiver direction	N-S	E-W	E-W
Shot direction	N-S	E-W	N-S
Shot spacing	10 m	20 m	12.5 m

Receiver spacing	10 m	10 m	25
Shot stack	2	2	-
Receiver line spacing	-	-	400 m
Shot line spacing	-	-	225 m
Geophone	5 Hz vertical component	5 Hz vertical component	5 Hz vertical component
Source type	Mini-vibe (6-ton)	Mini-vibe (6-ton)	Mini-vibe (6-ton)
Geodetic survey instrument	Differential Global Positions System (DGPS)	Differential Global Positions System (DGPS)	Differential Global Positions System (DGPS)

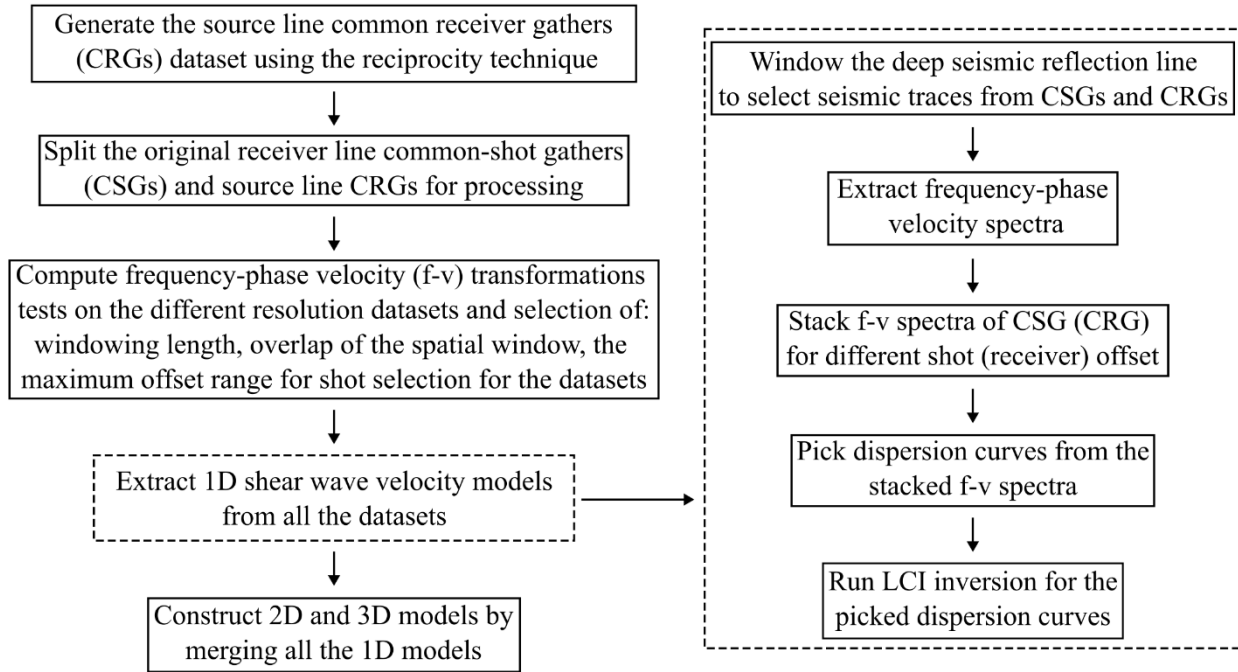
217

218 3.2 Data processing

219 The data were subdivided into three datasets: the two 2D lines (P1 and P2); nine E-W oriented receiver lines (R1-R9)
 220 from the 3D grid; and twenty-one S-N oriented source (shot) lines (S1-S21) from the 3D grid (Fig. 2b). The source
 221 line dataset was generated from the receiver line dataset by using the reciprocity principle to generate common receiver
 222 gathers (CRGs) along the source lines. The reciprocity principle states that a wavefield measured at point A generated
 223 by a point source located at point B is equal to the wavefield measured at point B generated by a point source located
 224 at point A (Knopoff and Gangi, 1959; Claerbout and Green, 2008; Katou et al., 2017). In seismic investigations, it
 225 illustrates that the same seismogram will be recorded if seismic source and receiver locations are interchanged,
 226 irrespective of the geometrical subsurface complexity, as long as the geometry of obstacles and other bodies in the
 227 vicinity of the source and receiver are fixed (Claerbout and Green, 2008). The implementation of the reciprocity
 228 theorem was achieved by selecting receivers situated along and near source lines and using them to generate CRGs
 229 by projecting waveforms recorded at the receivers to their respective shot locations.

230 The MASW technique was applied to the three seismic datasets described above using a workflow based on the
 231 method by Socco et al. (2009), where a moving spatial window is used along the seismic lines to retrieve a set of local
 232 SW dispersion curves (DCs). Figure 3 gives a schematic summary of the entire processing workflow. Generally, the
 233 raw data undergo a data preconditioning that consists of splitting the profiles characterized by severe sharp turns into
 234 separate segments close to straight lines, as severe profile crookedness distorts the phase shift variation between
 235 neighboring traces and results in spurious velocities (Lin et al., 2017). The optimal MASW processing parameters,
 236 i.e., spatial window length, overlap of the moving spatial window, and the maximum offset range for shot selection,
 237 were defined to obtain a good compromise between spectral and spatial resolution, and the optimal signal-to-noise
 238 ratio for the dispersion curve analysis by doing some tests (Socco et al., 2009). The spatial window needs to be long
 239 enough to ensure the recording of longer wavelengths of interest (i.e., the target depth) and small enough not to violate
 240 the homogeneous media assumption assumed underneath the receiver spread. Meanwhile, the minimum and maximum
 241 offset ranges are chosen such that they minimize near-and far-field effects and improve the signal-to-noise ratio. For
 242 each window position, the spectra resulting from different shots falling within the selected offset ranges were
 243 computed using the phase shift method (Park et al., 1998) and stacked to improve the signal-to-noise ratio of the
 244 dispersion image (Grandjean and Bitri, 2006; Neduczka, 2007). From the stacked spectra, the maximum spectral

245 amplitude at each frequency, deemed to correspond with the energy of the SW fundamental mode, was automatically
 246 searched to obtain the local DCs. The DCs were picked through an automatic maxima search and manual cleaning to
 247 ensure high-quality DC picks. The positions of the DCs were assigned as the center of the windows for which the
 248 dispersion spectrum was computed.



249

250 **Figure 3: Schematic summary of the entire processing procedure.**

251

252 In our case, the three datasets have different spatial sampling characteristics that lead to different processing parameter
 253 choices (Table 2). Due to the receiver spacing, which is 25 m for receiver lines, 12.5 m for shot lines, and 10 m for
 254 the 2D lines, the spatial windows used to process the data sets are large with respect to usual near-surface SW surveys.
 255 Typically, for near-surface investigations, data that are acquired on purpose for SW analysis would use receiver
 256 spacing of 2-5 m. In this case, we use the 3D seismic data acquired for deep exploration and the survey design is not
 257 optimized for SW. This imposes the use of processing windows larger than those generally used in traditional SW
 258 surveys, which could result in more local anomalies being suppressed. The spatial sampling is also critical, since a
 259 large spatial sampling can generate aliasing. In the present dataset, given the higher velocities and the limit on high-
 260 frequency content, we do not extract wavelengths smaller than the spatial sampling. Moreover, surface wave DCs can
 261 be extracted at wavenumbers beyond the Nyquist wavenumber (See Socco and Strobba, 2009 for details), hence we
 262 do not consider spatial aliasing a critical aspect for the processing. The 2D lines (P1 and P2) are those with the denser
 263 spatial sampling (10 m receiver spacing) and shot layout (10-20 m shot spacing). The utilization of a dense spatial
 264 sampling and shot layout allowed the attainment of high signal-to-noise spectra and broad band DCs on 250 m
 265 windows and a 200 m max offset range. While for the larger 2023 3D seismic survey profiles (i.e., receiver lines R1-

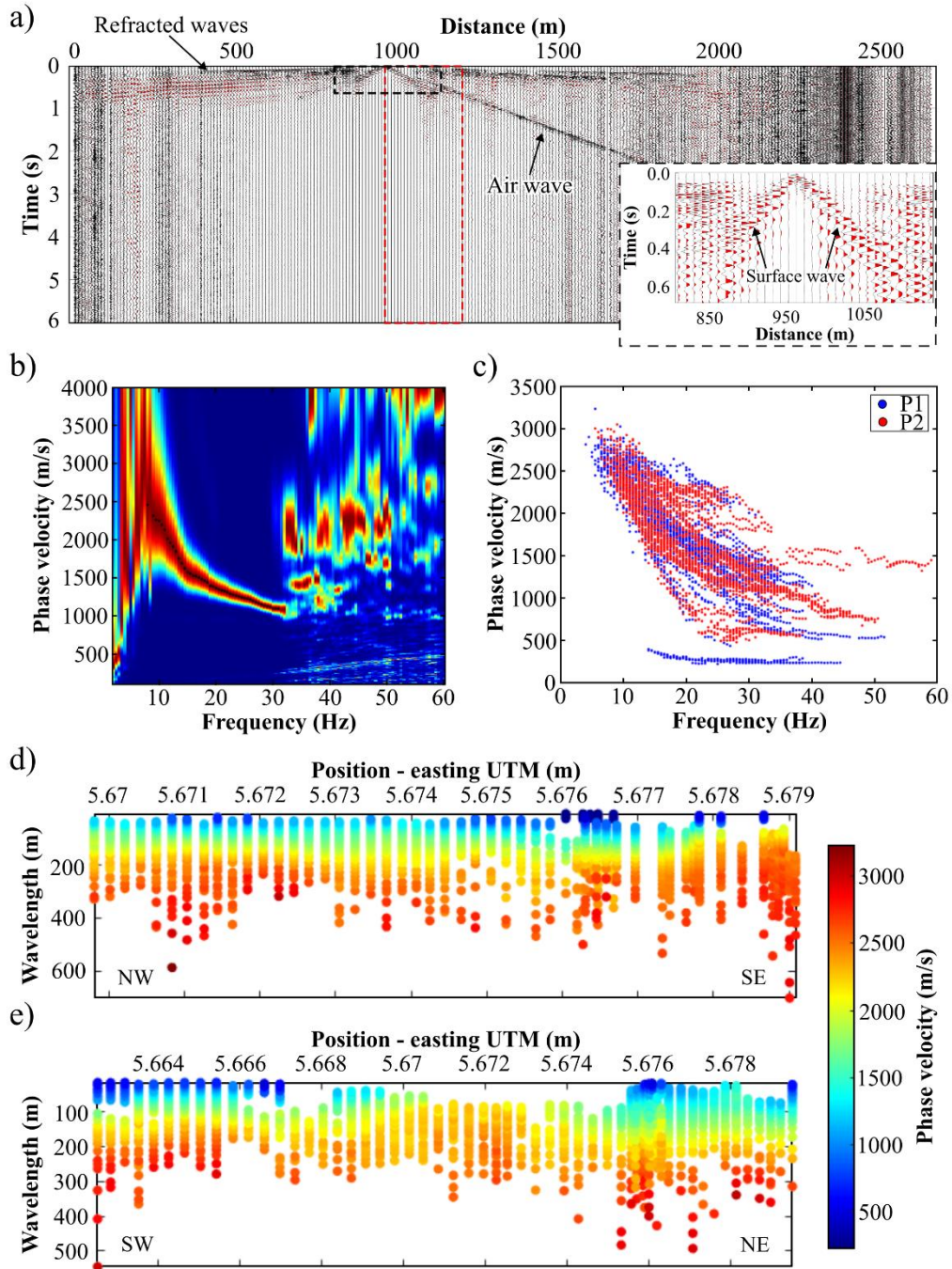
266 R9) the shortest window size that provided good quality DCs was 500 m. The shift of the moving window position
 267 was set equal to the receiver spacing and this led to different densities of DCs along the lines for the three datasets.
 268 For the two datasets extracted from the 3D grid, the most critical aspect was related to the small number of available
 269 sources in line with the receivers (or the opposite for the Common Receiver Gathers (CRGs)). The shot spacing along
 270 receiver lines is 225 m (distance between shot lines), while for the CRGs the “shot” spacing is 400 m (distance between
 271 receiver lines) leading to very limited stacking of the spectra.

272 **Table 2:** Windowing parameters used for the optimal dispersion curve extraction.

Processing parameters	2D Line	Normal 3D grid receiver lines	Reciprocity lines (source lines)
Minimum window size	250 m	500 m	125 m
Maximum window size	250 m	500 m	250 m
Window stride	10 m	25 m	12.5 m
Minimum offset	10 m	10 m	10 m
Maximum offset	200 m	400 m	400 m

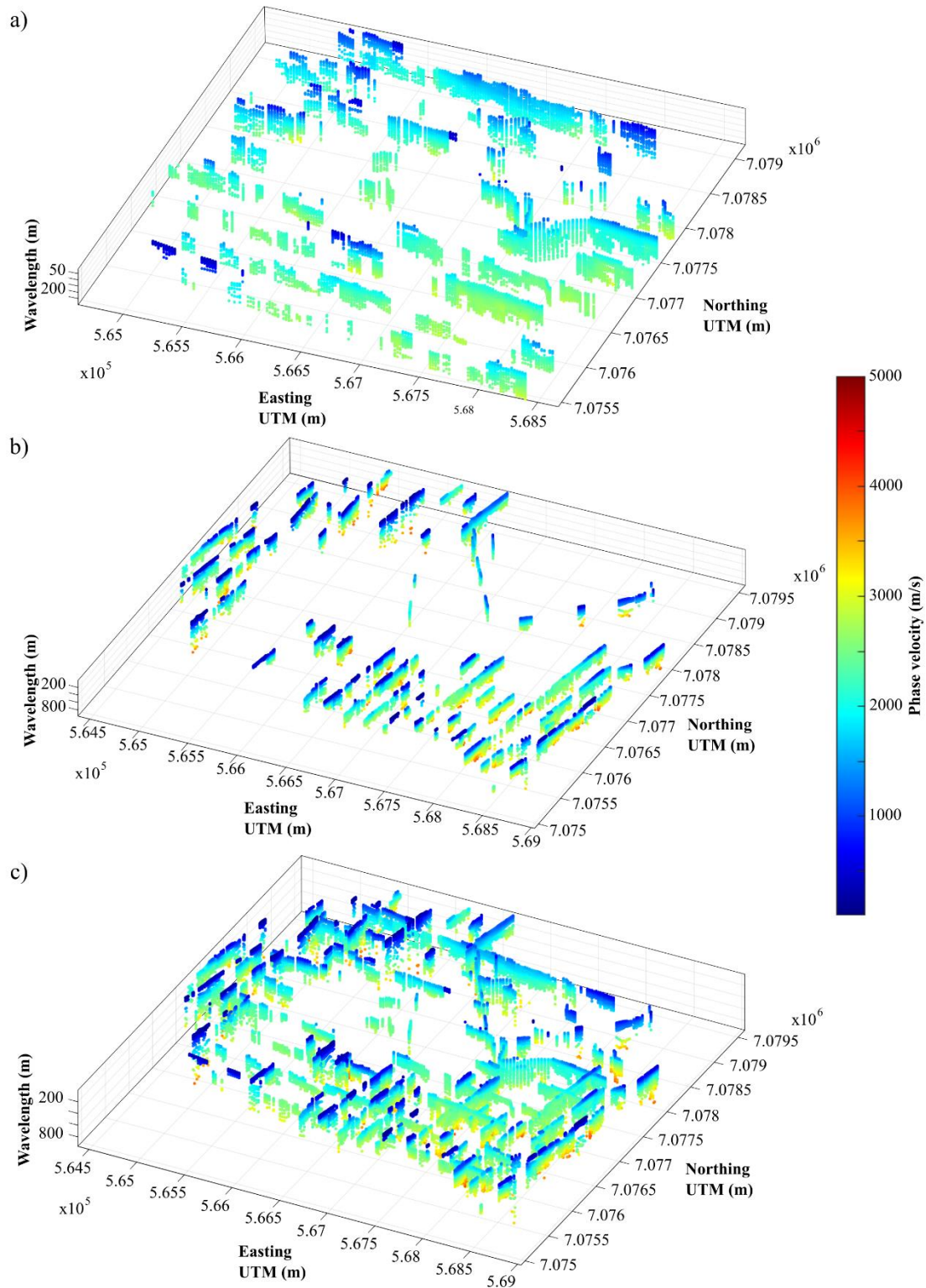
273

274 Figure 4a shows an example of a shot gather obtained in the study area, along profile P2. The seismic record in Figure
 275 4a contains a broad band ground roll that is visible at near-offset traces. Figure 4b gives the frequency-phase velocity
 276 spectrum obtained after transforming within the red dashed rectangle. The spectrum was obtained after stacking
 277 spectra from 5 different shots within the set offset range, where the DC (fundamental mode) is picked as the spectral
 278 maxima. Figure 4c shows all the picked DCs for P1 and P2, while Figure 4d and 4e display them as a function of
 279 wavelength at their spatial location along the lines. In Figure 4d and 4e, it is remarkable that long wavelengths, i.e.,
 280 high investigation depths, are achieved thanks to the high velocities prevalent at the site. Figure 5a, 5b, and 5c show
 281 the DCs that were picked along the 3D grid receiver lines, source lines, and receiver and source lines combined,
 282 respectively.



283

284 Figure 4: (a) Shot gather from the seismic profile P2, showing the window position (red dashed rectangle) that is later
 285 transformed into the frequency-phase velocity domain. A zoomed in window showing the surface wave trend visible in the
 286 record is shown, and its location is indicated using a dashed black rectangle. (b) Frequency-phase velocity spectrum from
 287 P2 obtained after transforming the highlighted data in Figure (a), where the black dots depict the picked dispersion curve.
 288 (c) Picked surface wave dispersion curves for profiles P1 (dark blue) and P2 (red), plotted as a function of frequency and
 289 phase-velocity. In (d) and (e), surface wave dispersion curves for profiles P1 and P2 are plotted as a function of wavelength
 290 depth and spatial location.

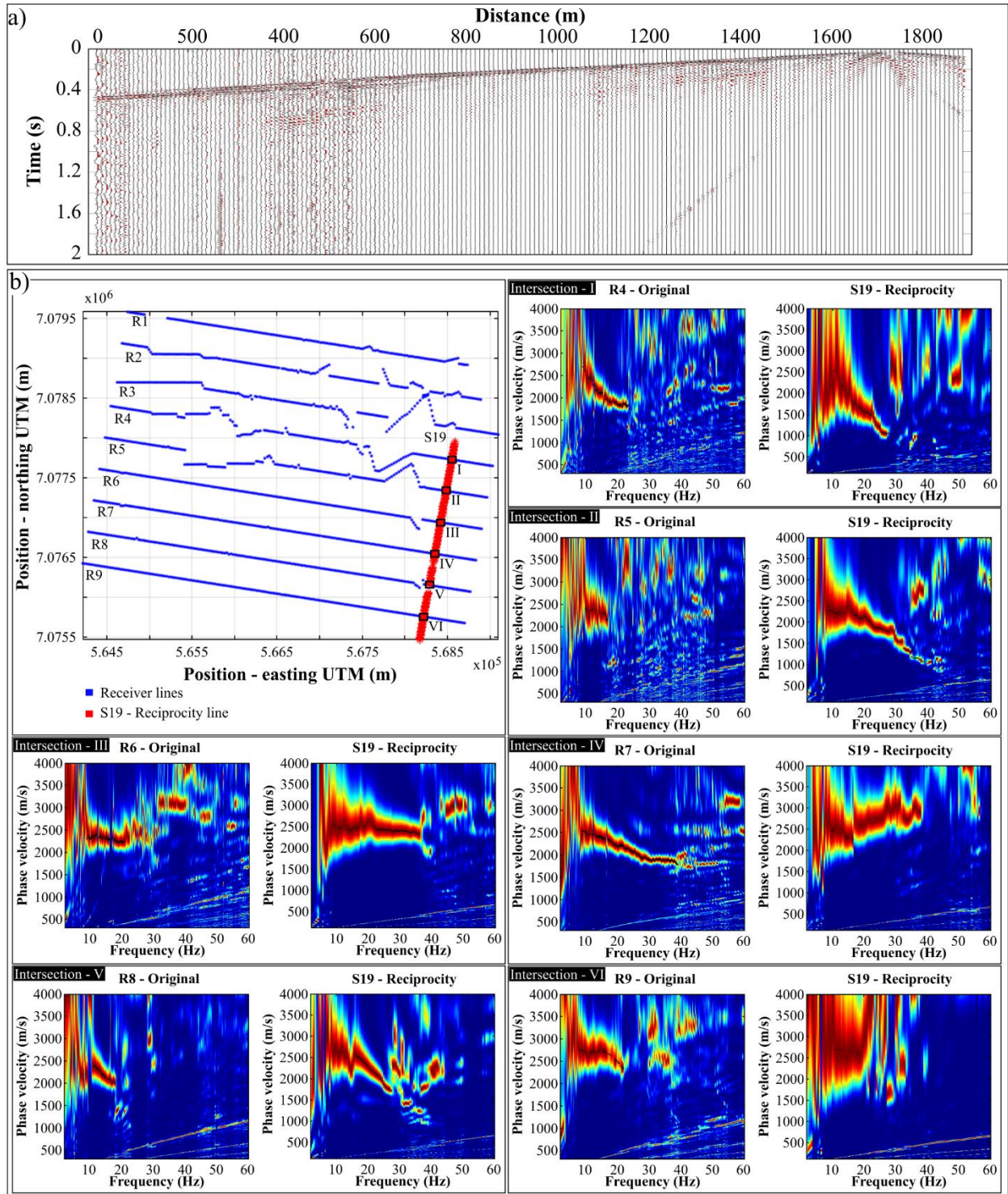


291

292 **Figure 5: Dispersion curves picked along the (a) receiver and (b) source lines. (c) Combined receiver and source line**
 293 **dispersion curves. The dispersion curves are plotted as a function of wavelength and spatial location.**

294 A total number of 2557 DCs were picked along the 3D grid; 767 of the DCs were extracted along receiver lines, while
295 1790 (more than twice) were extracted along source lines. The application of the reciprocity principle enabled the DC
296 density to be increased by $\sim 230\%$ rounding-off. In the retrieved DC datasets, gaps are present in areas: (1) where the
297 stacked spectra did not show a clear fundamental mode, thus no DC could be picked, which is possibly due to the
298 presence of sharp lateral variations within the subsurface, (2) where data could not be acquired due to the presence of
299 mining infrastructure (e.g., tailings dams, solar panels, satellites, roads, etc.), and (3) where source and receiver lines
300 are distorted by mining infrastructure.

301 Figure 6a gives an example of a CRG obtained for line S19. To validate the dispersion curves obtained from the CRG
302 processing, we compared the spectra located at the crossing point for source and receiver lines (Fig. 6b). The
303 comparison needs to be evaluated taking into consideration that the spectra are computed along two orthogonal
304 directions and therefore the considered wavefields sample different portions of the subsurface that, given the large
305 window length, can lead to different phase velocities. We therefore do not expect the spectra to be necessarily equal.
306 In general, there is a relatively good agreement between the spectra of the two orthogonal lines and spectra computed
307 from CRGs are broader band than those computed along receiver lines. This is attributed to the traces in CRGs having
308 a smaller spacing (Table 1). Meanwhile, the spectra from the receiver lines have greater spectral resolution due to the
309 spectra along these lines being computed using larger spatial windows.

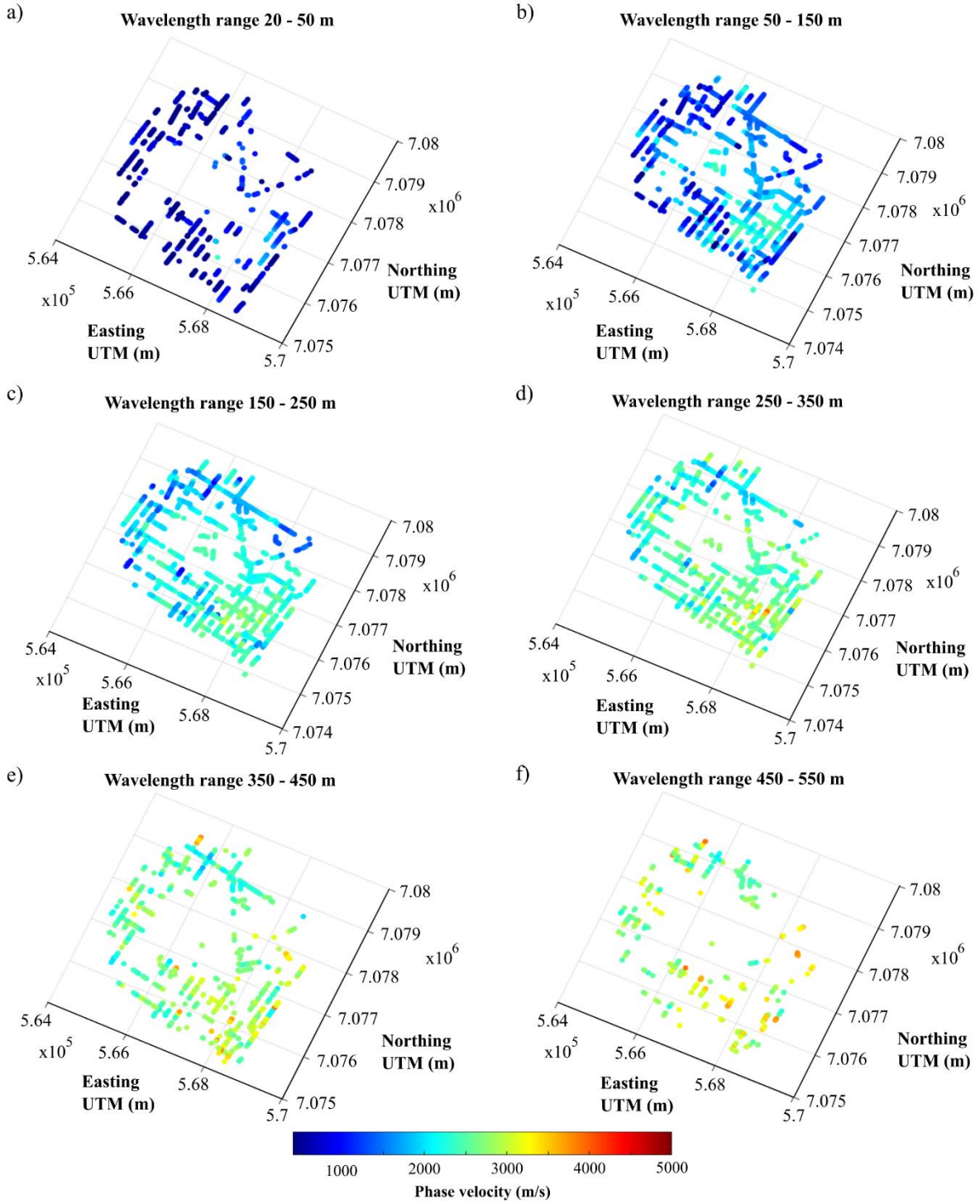


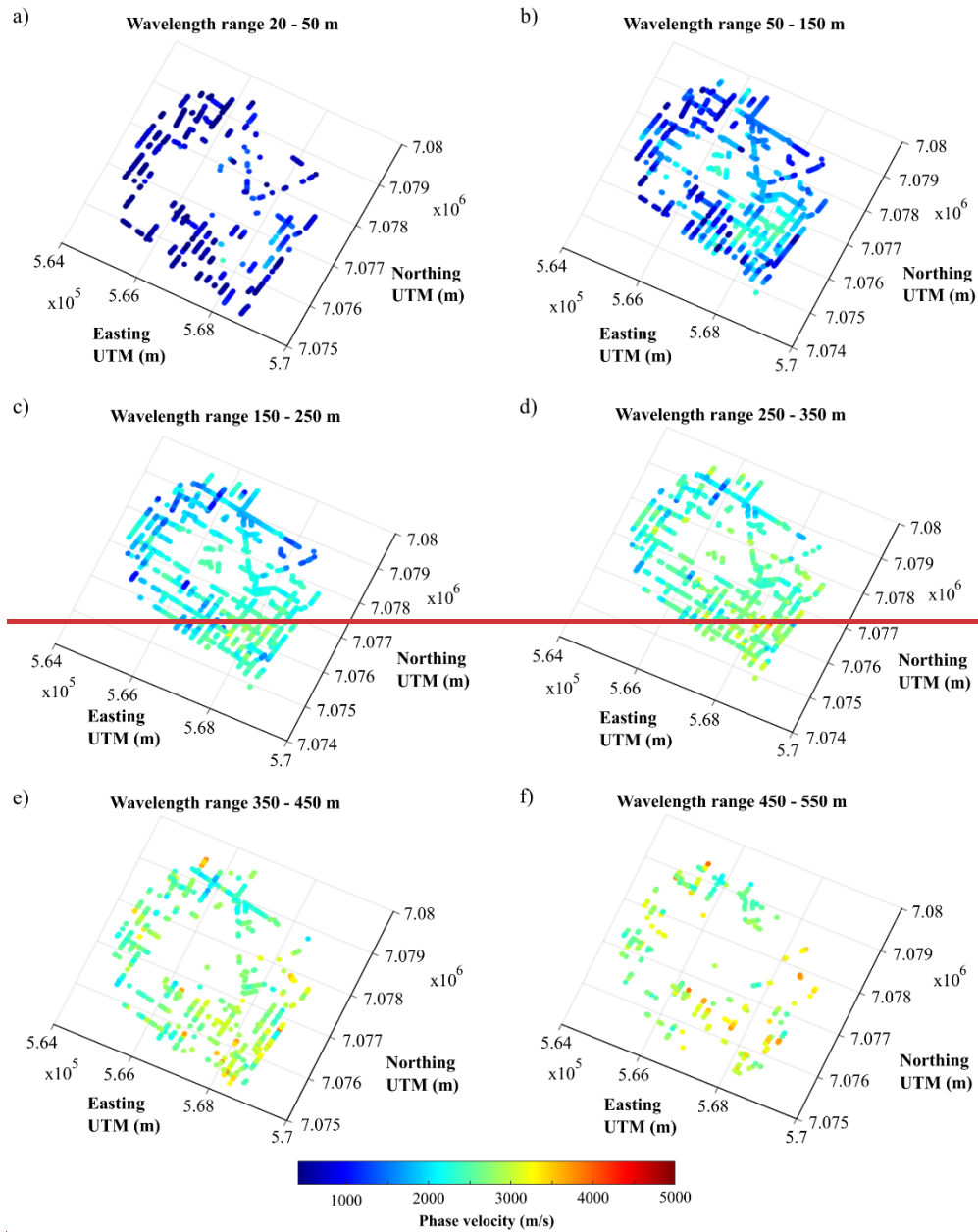
310

311 Figure 6: (a) Example of a common receiver gather obtained along source line S19. (b) Receiver and source line f-v spectra
 312 obtained at intersection locations I-VI.

313

314 In Figure 7a-f, we show the wavelength coverage of the estimated DCs for the 3D grid as pseudo-slices within different
315 wavelength ranges, i.e. for progressively higher investigation depths. The highest coverage is achieved for
316 wavelengths between 50 m and 350 m, but it is still significant up to 550 m over wide areas of the grid.





318

319 **Figure 7: Pseudo-slices of the estimated dispersion curves from the site shown using wavelength ranges of (a) 20 - 50 m, (b)**
 320 **50 - 150 m, (c) 150 - 250 m, (d) 250 - 350 m, (e) 350 - 450 m, and (f) 450 - 550 m.**

321

322 **3.3 Laterally constrained inversion (LCI)**

323 To invert the picked DCs for S-wave velocities, we adopted the LCI scheme. The LCI was first proposed by Auken
 324 and Christiansen (2004) for inverting resistivity data using a pseudo-2D layered parameterization. The LCI is a
 325 deterministic inversion technique that is predicated on an algorithm created for a 1D scheme that makes use of lateral
 326 constraints. A lateral constraint is a parameter that defines the variance permitted for parameters of neighbouring

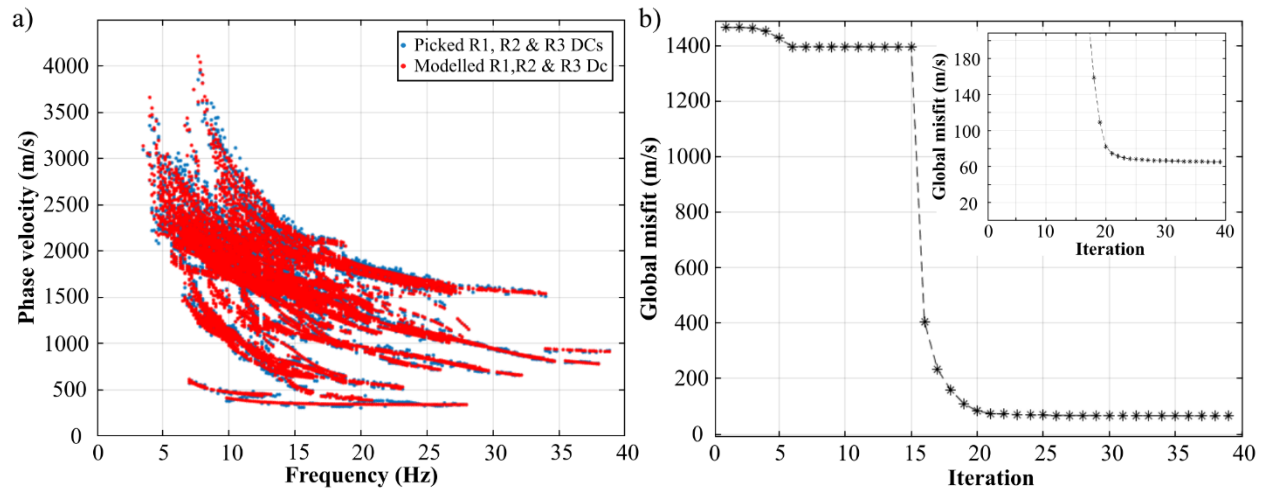
327 models (Wisén and Christiansen, 2005; Socco et al., 2009). The constraints represent a spatial regularization that
 328 avoids overfitting the final model. The smaller the expected variance in the area, the stronger the lateral constraints
 329 (Wisén and Christiansen, 2005; Socco et al., 2009). The optimization of the lateral constraints can be done by running
 330 a set of inversions starting from unconstrained and rising gradually the level of constraints until the fitting between
 331 model and data starts to decrease (Boiero and Socco, 2010). The inputs are the DCs and the initial model at the
 332 locations of the DCs. The initial model parameters of the LCI inversion scheme are the layer thicknesses, Poisson's
 333 ratio, density, and S-wave velocities. The technique simultaneously inverts all the picked DCs by minimizing a
 334 common objective function, which incorporates the fitting of data with the model, a priori information, and constraints.
 335 The LCI uses a damped least-squares inversion scheme to update the model iteratively. The initial S-wave velocities
 336 and layer thickness are updated after each iteration, while layer densities and Poisson's ratio are kept fixed (Khosro
 337 Anjom et al., 2024). The final result of the LCI is a S-wave pseudo-2D/3D velocity model.

338 In this study, the parameterization of the initial model is laterally invariant, Table 3, and is based on the obtained SW
 339 information and expected geological properties of the site: The initial S-wave velocity model was created from the
 340 picked DCs, while Poisson's ratio and density measurements were estimated based on the materials expected in the
 341 study area (i.e., mainly the partially metamorphosed sedimentary rocks of the Timeball Hill Formation). The maximum
 342 depth of the initial model was set on the basis of a sensitivity analysis with Montecarlo inversion and a wavelength-
 343 depth analysis (Socco et al., 2017) carried out on some sample curves (not shown here). The analysis computed the
 344 relationship between wavelength and investigation depth of the selected DC and showed that DCs with large
 345 wavelengths (Fig. 8e and 8f) have a large investigation depth that goes beyond 300 m. After some inversion tests, we
 346 used a lateral constraint of 700 m/s, which was the maximum level of constraint that could invert the data without
 347 overfitting the picked DCs (Fig. 8a). Figure 8 illustrates an example of the fitting obtained between picked and
 348 modelled DCs for lines R1, R2, and R3 (Fig. 8a), along with the global misfit calculated between the computed and
 349 experimental DCs for each iteration (Fig. 8b). The lowest global misfit obtained after 39 iterations is 65 m/s.

350 **Table 3:** Initial model parameters used to invert the picked dispersion curves.

Layers	S-wave velocity (m/s)	Density (g/cm^3)	Poisson's ratio	Thickness (m)
1	1000	1.8	0.3	20
2	1020	1.8	0.3	30
3	1200	1.8	0.3	30
4	1500	1.8	0.3	30
5	1500	1.8	0.3	30
6	1700	1.8	0.3	30
7	2000	1.8	0.3	30
8	2500	1.8	0.3	50
9	3000	1.8	0.3	100

351



352

353 **Figure 8: (a) Fitting between picked and modelled (from last iteration) R1, R2, and R3 dispersion curves. (b) Global misfit**
 354 **between the picked and modelled dispersion curves in (a). The inset in (b) shows a zoomed section of the global misfit.**

355

356 **4 Results and interpretation**

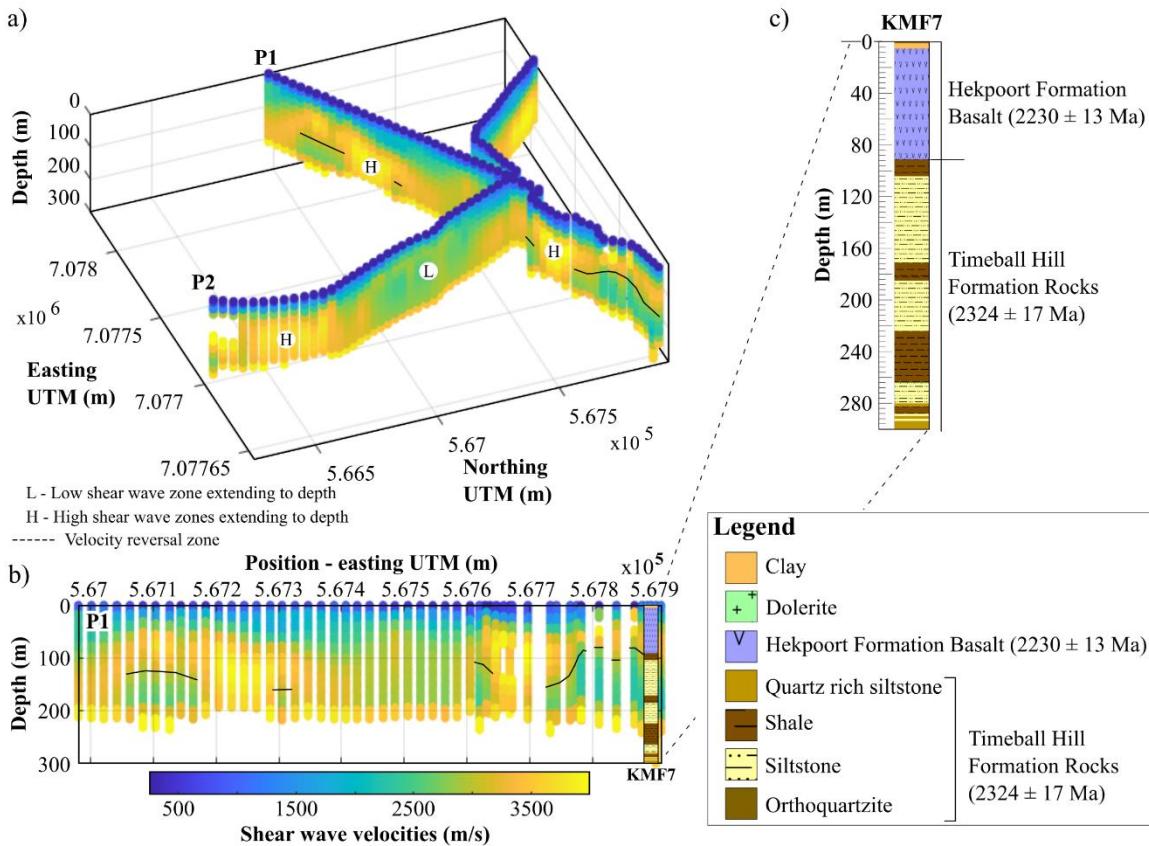
357 Figures 9 and 10 show the near-surface S-wave velocity models obtained through the LCI of the picked DCs along
 358 the 2D lines (P1 and P2) and 3D grid, i.e., along the receiver and source lines, respectively. In Figures 9, 10, and 11,
 359 both vertical and lateral velocity geological variations in the study area are resolved.

360 The results of the inversion showed significant update with respect to the initial model, as confirmation of the
 361 sensitivity of the data to model parameters. Velocity reversal zones with spatial consistency appeared in several zones
 362 of the final 2D/3D models. Since the initial model does not contain any velocity reversal, we consider them a reliable
 363 feature in the final models. The spatial consistency of the velocity of the layers is not due to the introduction of the
 364 lateral constraints since the low velocity zones were present also in the unconstrained inversion we carried out as a
 365 benchmark to define the optimum level of constraints. As far as the investigation depth is concerned, we tested the
 366 sensitivity through the wavelength-depth analysis and, in certain zones of the final velocity models, we saw significant
 367 updates with respect to the initial model, down to a depth greater than 300 m. In other zones, instead, a lower
 368 penetration depth was reached. We hence plotted the final models using a variable depth, based on the penetration
 369 depth of the DCs. The estimated velocities are in line with the expected values for the formations. The expected
 370 vertical resolution is ~ 20 m in the upper part of the model and ~ 40 m in the deeper part of the model, consistent with
 371 the selected initial model. The lateral resolution is related to the DC density along the line (from 10 to 25 m) but is
 372 also affected by the smoothing effect of the processing windows (125-500 m) (Table 2).

373

374 **4.1 Lithological layering, faults, and intrusions**

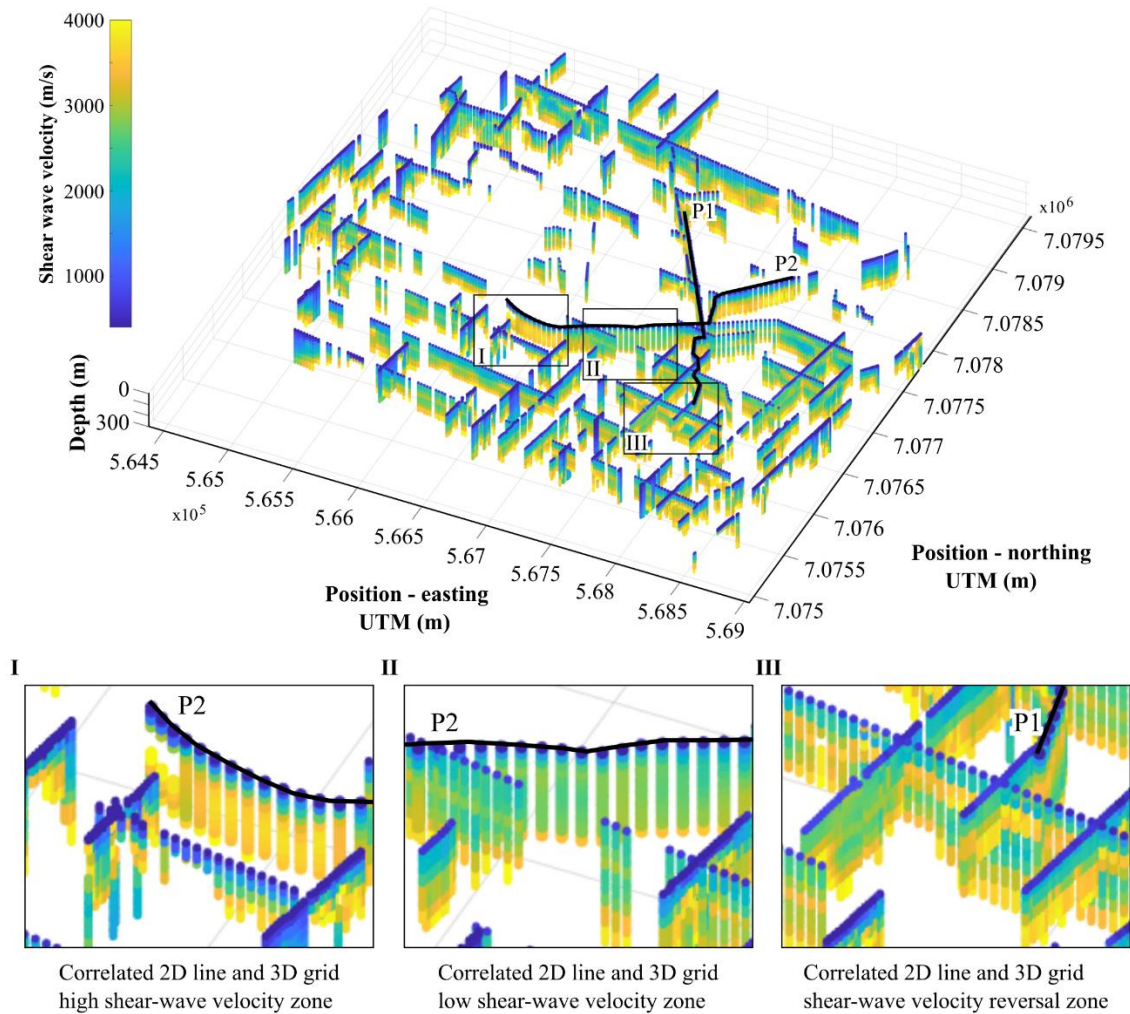
375 From the obtained high-resolution 2D S-wave velocity models, for P1 and P2 (Fig. 9), notable is that the site is
 376 characterized by a prominent (1) velocity reversal zone (indicated with a black solid line) due to lithological changes
 377 (Fig. 9b and c) and (2) low- and high-velocity zones that extend from the surface to great depths (i.e., > 150 m).
 378 Evident in Figure 10 is that the S-wave high (I), low (II), and reversal (III) velocity anomalies are also resolved in the
 379 3D grid S-wave velocity model. A good anomaly spatial location and velocity correlation is observed between the 2D
 380 and 3D models within the high-velocity, low-velocity, and velocity reversal zones (Fig. 10). In the 3D S-wave velocity
 381 model, the velocity reversal zone is overlain by a high-velocity zone with a sheet-like geometry (i.e., near-horizontal
 382 and planar-orientated, Fig. 10).



383

384 **Figure 9: (a) 3D plot of the high-resolution 2D shear-wave velocity models (i.e., P1 and P2). (b) P1 pseudo-2D S-wave velocity**
 385 **models shown along with the borehole (i.e., KMF7) located along the line. (c) Zoomed image of the borehole KMF7 showing**
 386 **the depth scale, formations, and rock types located in the area.**

387



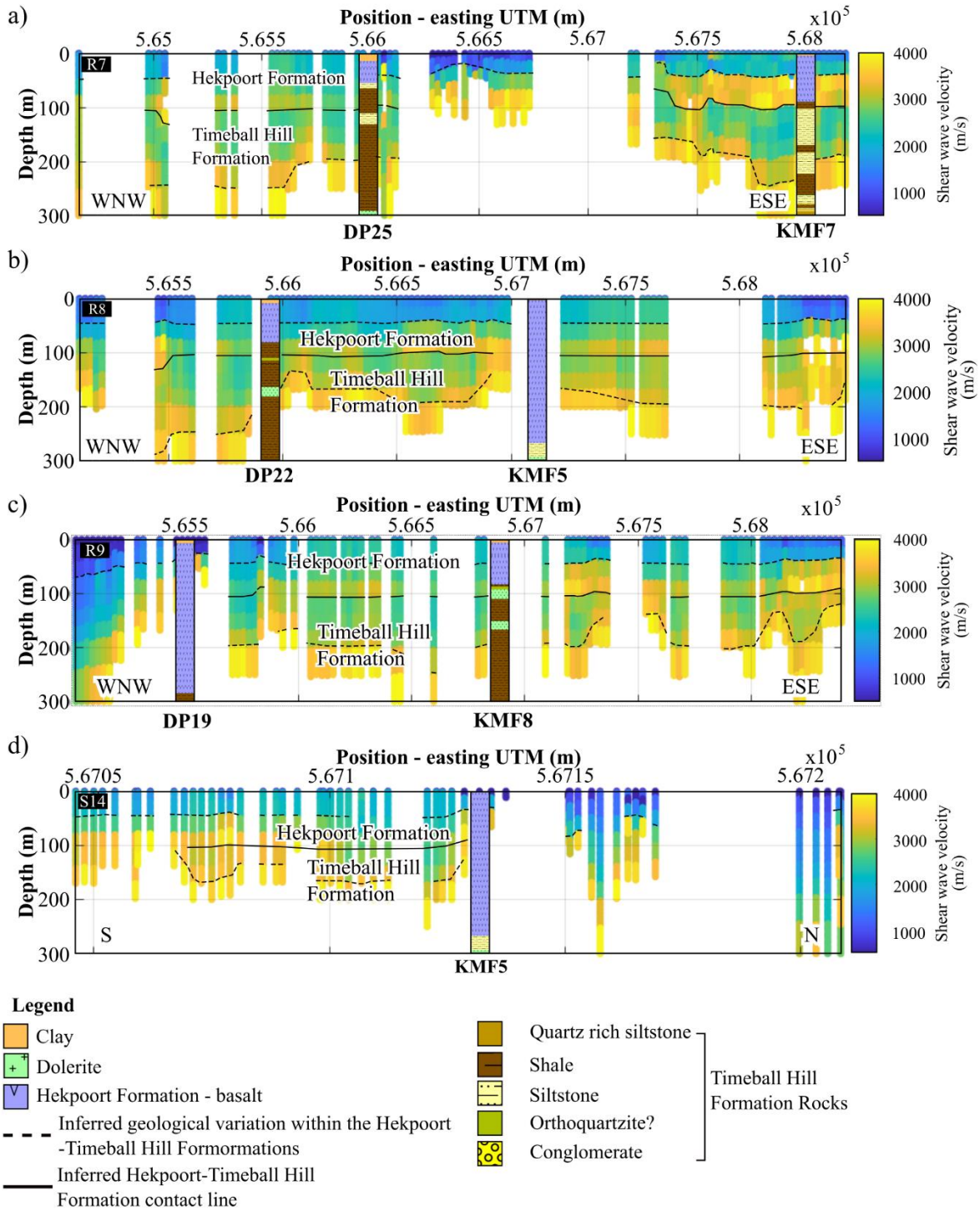
388

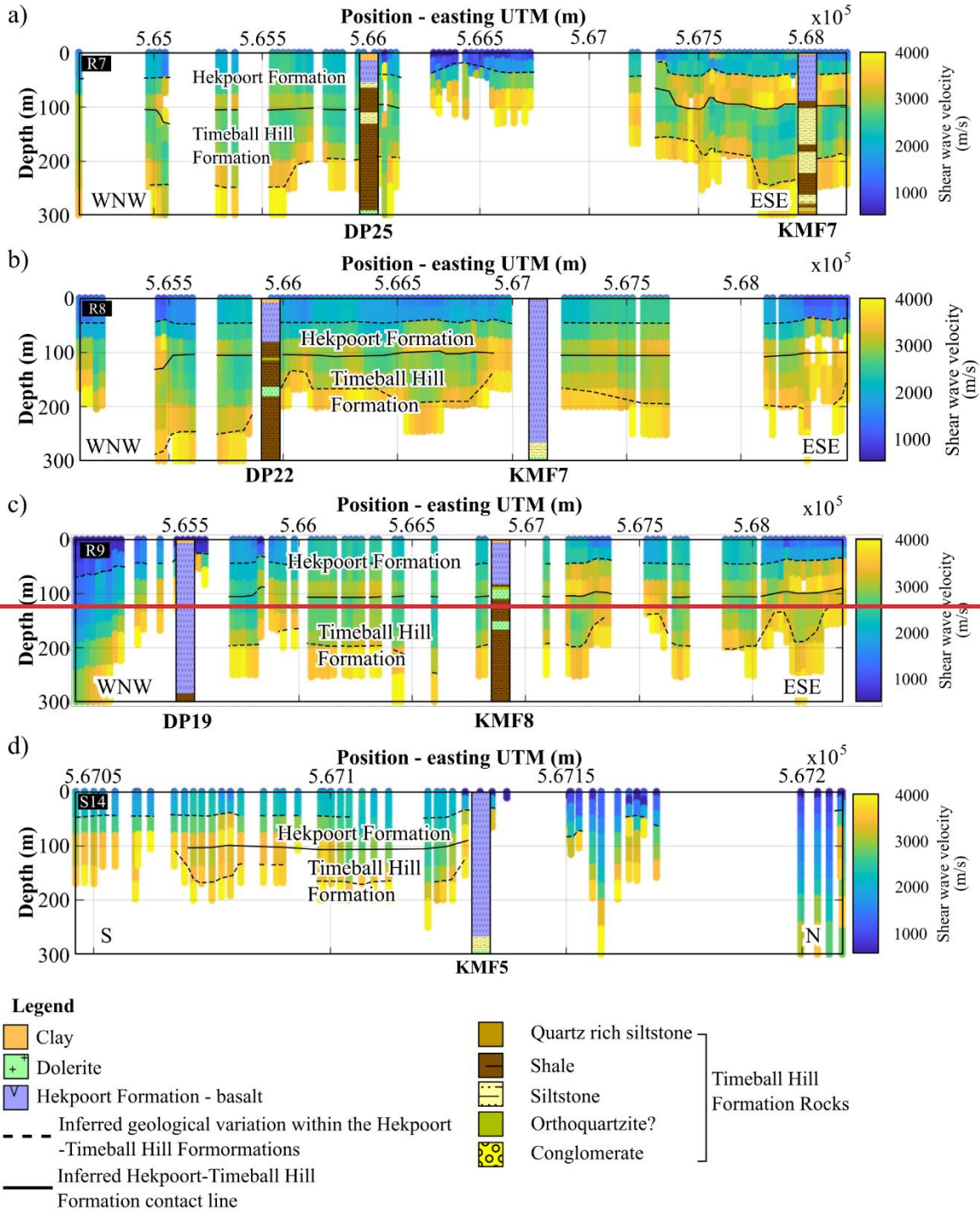
389 **Figure 10: South Deep Gold Mine 2D and 3D grid data plot. The rectangles I, II, and II indicate correlating high, low, and**
 390 **velocity reversal zones between the obtained 2D and 3D S-wave velocity models, respectively.**

391

392 Figure 11 illustrates the correlation between available surface borehole logs in the study area and the S-wave velocity
 393 profiles closest to them. Apparent in Figures 9b, c, and 11a is that the identified velocity reversal zone (indicated by
 394 a solid black line) marks the boundary/contact between the overlying basalts of the Hekpoort Formation and the
 395 underlying shales and siltstones of the Timeball Hill Formation. Also notable in Figures 9b, 11a and b is that where
 396 the depth extent of the uppermost Hekpoort Formation rocks is greater than ~ 50 m and less than ~ 200 m, the contact
 397 between the Hekpoort Formation and Timeball Hill Formation is mapped relatively well; while in areas where the
 398 thickness of the Hekpoort Formation is greater than ~ 200 m (Fig. 11b and c), the Hekpoort-Timeball Hill Formation
 399 contact cannot be resolved. Indicated by the black dashed lines are the significant lateral variations present within the
 400 rocks of the Hekpoort and Timeball Hill Formations, which are elaborated more in the following section. This

401 comparison of S-wave velocity profiles and proximal borehole information illustrates that the obtained S-wave
402 velocities are sensitive to the lithological variation characteristic of the site and are reasonable and reliable.





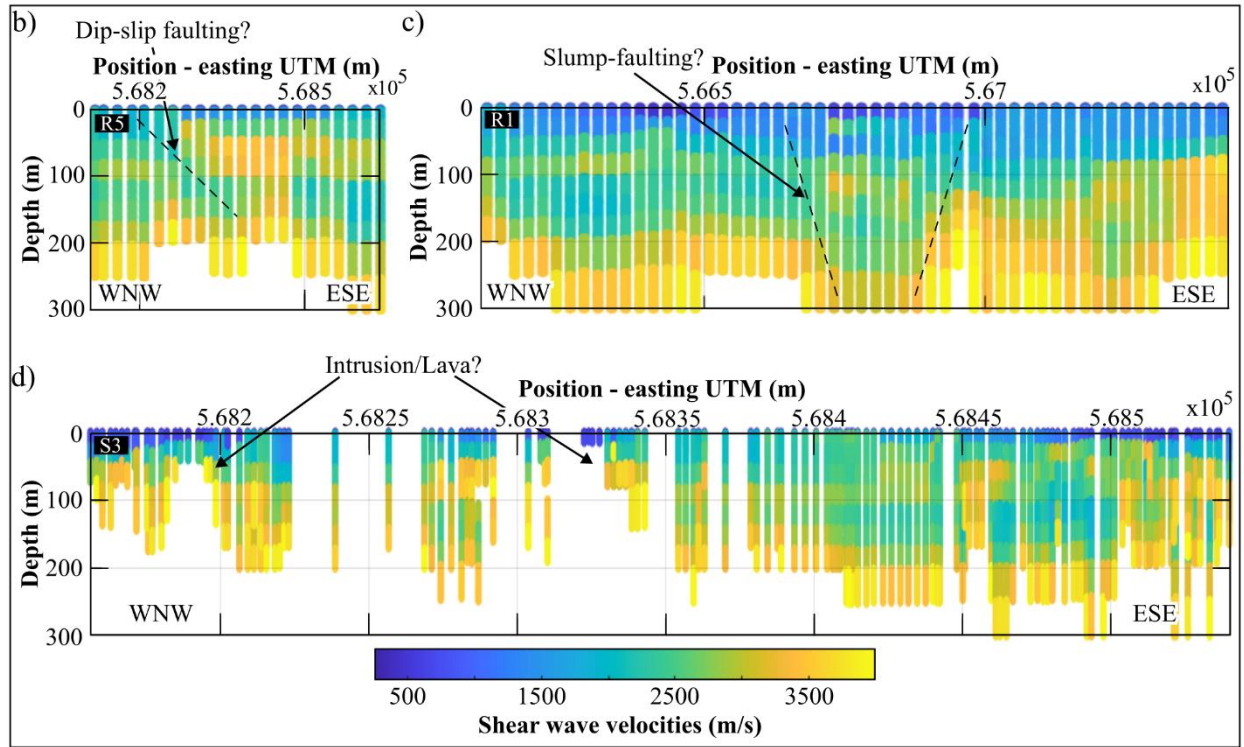
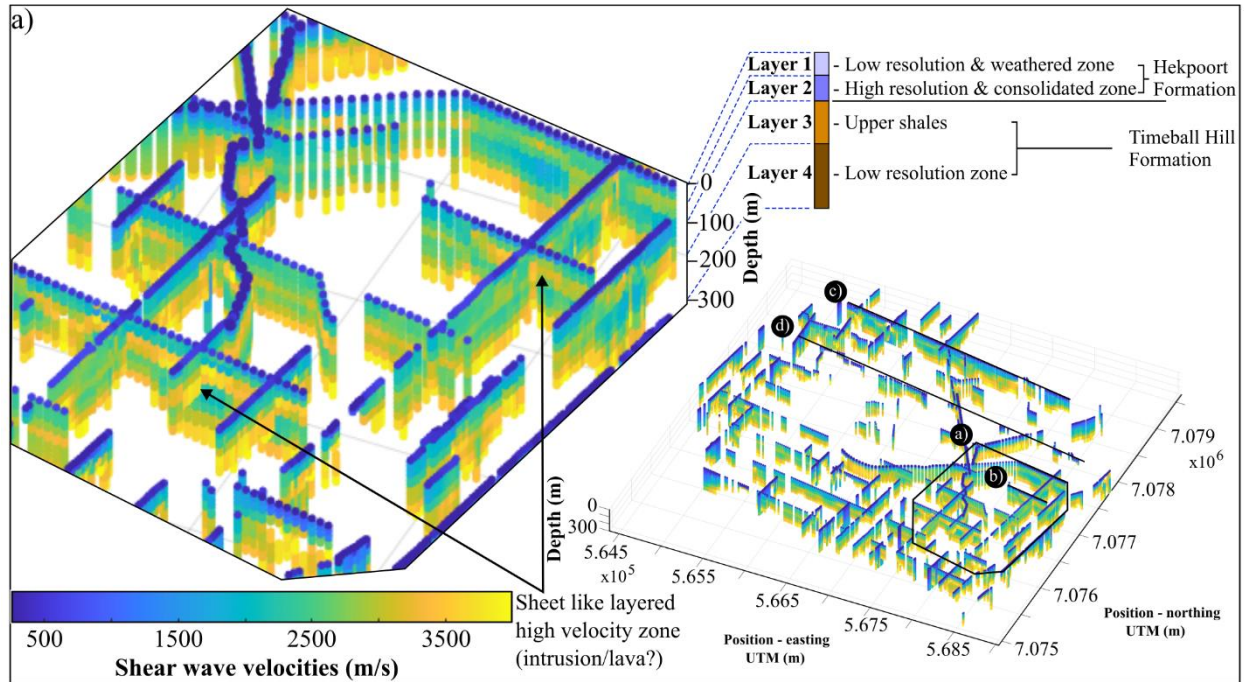
404

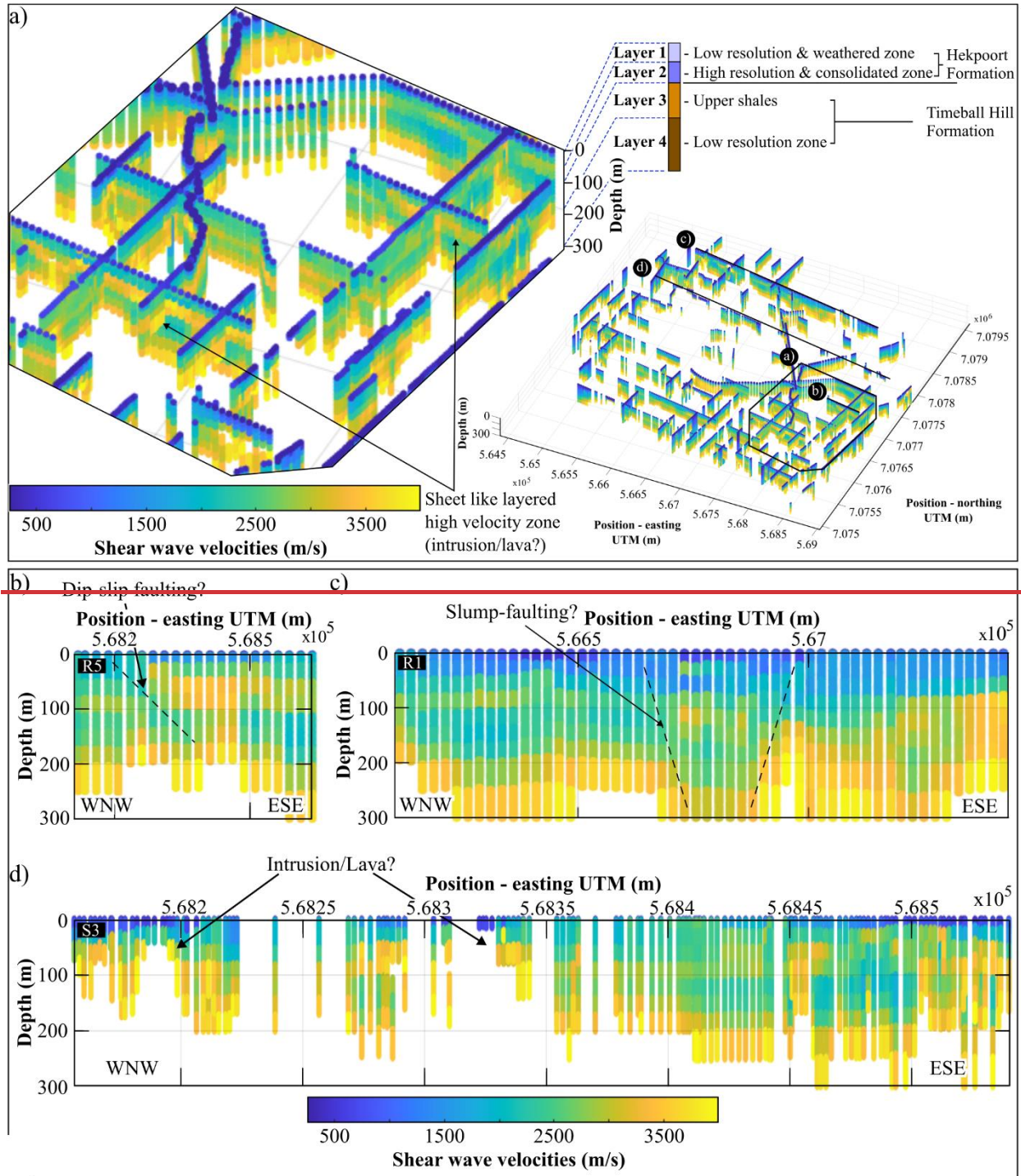
405 **Figure 11: Representative boreholes of the study area projected on pseudo-2D S-wave velocity models constituting the 3D**
 406 **grid that are closest to them. Pseudo-2D S-wave velocity models of lines: (a) R7, (b) R8, (c) R9, and (d) S14.**

407

408 In general, within the top 300 m of depth, the overall S-wave velocity is interpreted to show four sheet-like subsurface
 409 layers (Fig. 12a). The first layer roughly extends from the surface to a depth of ~ 40 m and has S-wave velocity ranging

410 from < 500 m/s to ~ 2500 m/s. The second layer shows higher velocities (~ 2500 m/s to ~ 3500 m/s) and extends from
411 ~ 40 m to 120 m below the surface. A third layer, with S-wave velocities similar to the first one, extends from ~ 120
412 m to 200 m. The last resolvable layer is a high-velocity zone (> ~3500 m/s), extending from ~ 200 m of depth (Fig.
413 12a). The first two identified layers belong to the Hekpoort Formation and are interpreted to constitute the weathered
414 and least weathered zones of the Hekpoort Formation rocks, respectively. The last two layers belong to the upper
415 shales of the Timeball Hill Formation; the high velocities in the second layer of the Timeball Hill Formation are
416 attributed to the presence of sills at those depths, see Figure 2c. During the emplacement of ultramafic-mafic rocks of
417 the Transvaal Supergroup, shale- and quartzite-dominated formations (i.e., Timeball Hill, Boshhoek, and Daspoort
418 Formations) formed preferential sill emplacement locations as compared to the carbonate and volcanic formations of
419 the Supergroup. The shales and quartzite formations, being preferential emplacement locations, are linked to the
420 abundant parting surfaces within shales (i.e., fissility) and the prevalent upper and lower contacts between thick
421 quartzites with under- and overlying-shales (Button and Cawthorn, 2015). The transition from the basaltic Hekpoort
422 Formation rocks (high seismic velocity rocks) to the metasedimentary rocks of the Timeball Hill Formation (low
423 seismic velocity rocks) results in the velocity reversal zone observed between the second and third layers, indicated
424 by a solid black line in Figures 9 and 11. Considered, however, is that the presence of a velocity reversal results in a
425 reduction in the reliability of S-wave velocities of layers located below the reversal zone. Velocity reversal zones
426 reduce the penetration of large wavelengths into the underlying layers since the wavefield energy is trapped into the
427 low velocity layer, thus reducing the mapping resolution and velocity reliability at depth (Groves et al., 2011).
428 Additionally, SW analysis suffers from a reduction in resolution with depth and, due to this, not much interpretation
429 is drawn on the exact S-wave velocities observed within the last layer. The prevalence of the velocity reversal zone
430 throughout the study area suggests that the Hekpoort Formation is present throughout the vicinity of South Deep Gold
431 Mine, contrary to what is observed in the local geological map of the area (Fig. 1c). This is supported by the presence
432 of Hekpoort Formation basalts in areas where Timeball Hill Formation rocks are reported to be outcropping (see
433 boreholes KMF5, KMF6, and KMF7 in Figure 1c). However, the confirmation of this interpretation is hampered by
434 the lack of available borehole data around the center and northern area of the mine. The depth, thickness, and S-wave
435 velocities of the imaged lithologies and corresponding layers are variable, and in some areas, are disturbed by low and
436 high-velocity zones that extend from the near-surface to depths beyond that resolved by the survey (Fig. 12b-d). These
437 high- and low-velocity zones are discussed in the following section.





439

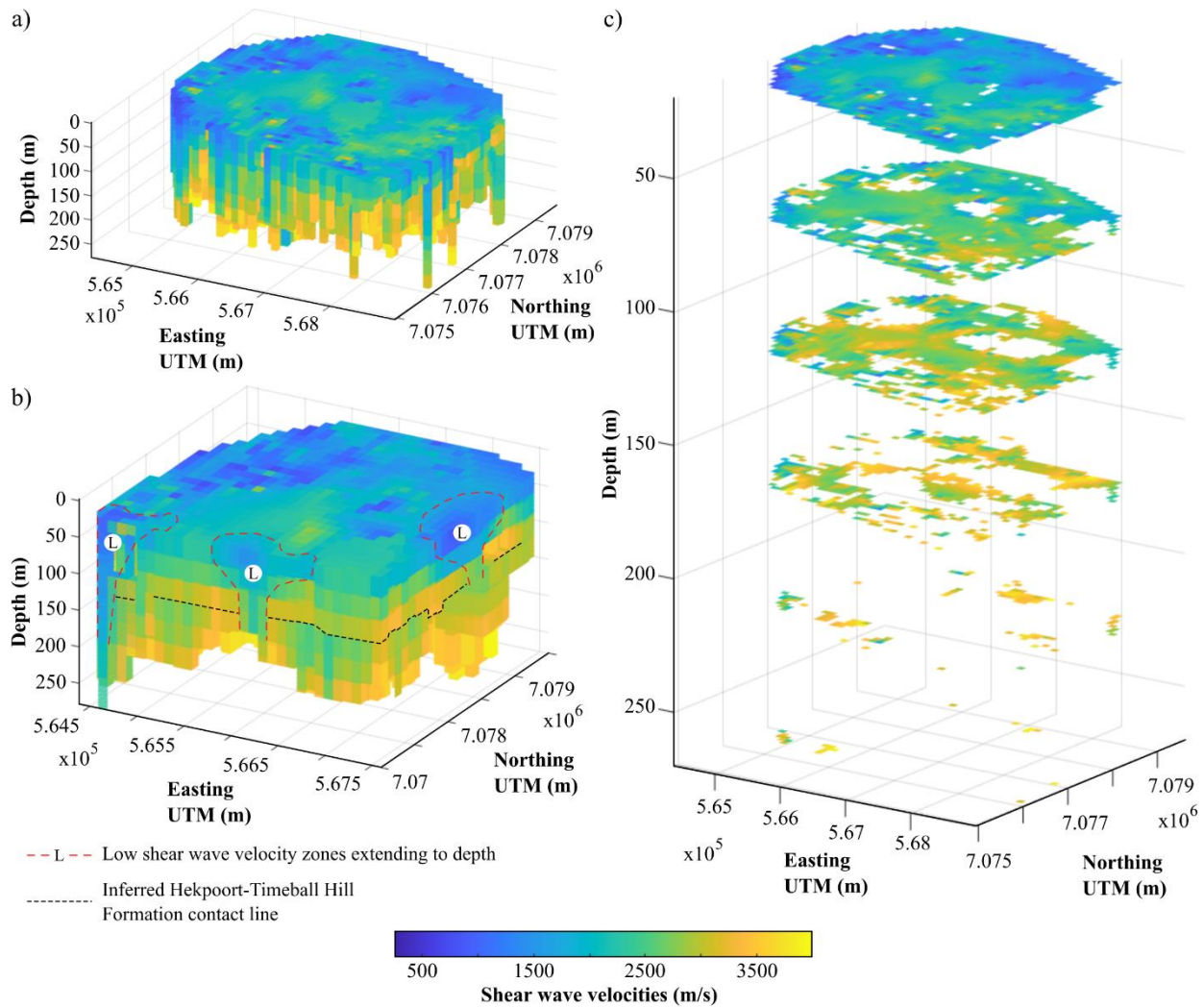
440 Figure 12: Local features observed at the site. (a) Sheet-like layering; (b) dip-slip faulting; (c) slump-faulting; and (d)
 441 intrusions/lavas. Shown in the 3D grid in (a) are the locations of the zoomed in 3D grid displayed in (a) and the locations of
 442 the S-wave velocity sections in (b), (c), and (d), respectively.

443

444 The low-velocity zones are interpreted to be associated with dip-slip (Fig. 12b) and slump-faulting (Fig. 12c). The
445 reduction in S-wave velocities within fault zones is attributed to increased fracturing, porosity, and fluid content,
446 which lead to the physical breakdown (weathering and alteration) of the primary minerals in the in-situ rock into less
447 dense secondary phases. This transformation reduces the rock's elastic moduli, ultimately lowering seismic velocities.
448 According to Mutshafa et al. (2023), weathering of the rocks in the study area is highly variable and can extend to
449 depths greater than 500 m, which is consistent with the presented findings. The interpreted dip-slip faulting, in Figure
450 12b, shows relative vertical displacement between the rocks above and below the fault plane. Meanwhile, the slump-
451 faults, Figure 12c, are largely characterized by wide near-surface footprints that taper down with depth, i.e., they
452 progressively get narrower with depth. In the slump zone, the layers (including the overlying volcanic rock layers)
453 are observed to be sunken. The identified faulting and possible intrusions are characteristic of the study area and
454 consistent with the findings of Cousins (1962) and Parsons and Killick (1990). Cousins (1962) documents that the
455 rocks of the Pretoria Group are displaced by post-Pretoria Group faults that displace both the Pretoria Group rocks
456 and the base of the Transvaal Supergroup, and slump-faulting, which only affects the formations within the Transvaal
457 Supergroup, but not the base of the Transvaal Supergroup. Cousins (1962) interpreted these faults as slump-faulting
458 originating from the subsidence of the dolomitic units of the Transvaal Supergroup, situated within a formation
459 underlying the Pretoria Group Formations.

460 High-velocity zones, extending from the near-surface to depth or terminating within the upper subsurface, are observed
461 in Figures 9a, 10, and 11b–d. In Figure 11b–d, these zones correlate with thick basaltic lava flows of the Hekpoort
462 Formation. The termination of S-wave velocities at depth reflects the penetration depth and the influence of complex
463 structural features and abrupt lithological heterogeneities.

464 Figure 13a-c illustrates the interpolated 3D model view of the grid acquired at the mine and depth slices (i.e., velocity
465 maps) extracted from the 3D model. Figure 13a displays the velocity model of the survey area in 3D. The zones
466 marked by dashed red lines in the vertically sliced 3D model, Figure 13b, illustrate the coherency and depth extent of
467 the low-velocity zones in the area and their interaction with the reversal zone (shown using a black dashed line and
468 situated at a depth of ~ 120 m). The velocity maps in Figure 13c better illustrate the increase of velocities with depth
469 and the presence of low-velocity zones that extend from the near-surface to greater depths.



470

471 **Figure 13: (a) 3D S-wave velocity model of the study area. (b) Cropped 3D S-wave velocity model showing the velocity**
 472 **reversal zone (indicated by the black dotted lines) and low velocity zones that extend from the surface to greater depths**
 473 **(indicated by the red dotted lines). (c) 3D S-wave velocity model depth slices illustrating the general variation of S-wave**
 474 **velocities with depth.**

475

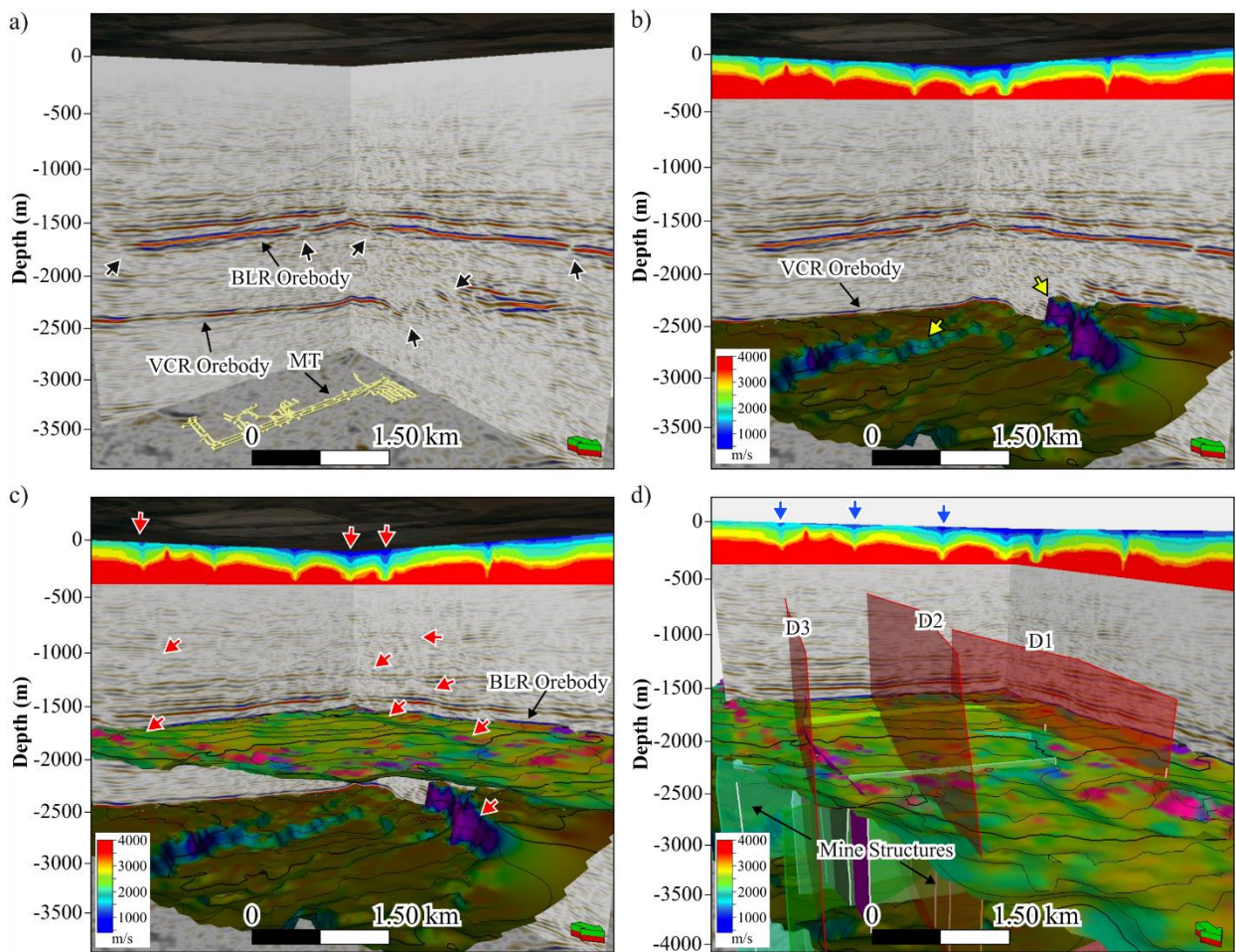
476 4.2 Structural linkage between shallow aquifers and deep mining levels

477 To investigate the structural geology linkage between shallow aquifers and deep mining levels, we integrated our
 478 shallow 3D Vs model with the legacy 2003 3D reflection seismic data acquired for deep gold exploration, mine
 479 planning, and development (Fig. 14a-d). The legacy 3D seismic survey covers both the South Deep Gold Mine and
 480 Kloof Gold Mine and was primarily acquired to map the VCR orebody and major fault systems (Manzi et al., 2012a).
 481 The base of the 2.65–2.05 Ga Neoproterozoic–Paleoproterozoic Supergroup horizon (Black Reef, ~ 0.5 km below ground
 482 surface) and the mine orebody (VCR, ~ 3 km below ground surface) are well-defined by the legacy 3D seismic data

483 (Fig. 14a-d). Both the VCR orebody and the base of the Transvaal Supergroup (i.e., BLR orebody) are cross-cut by
484 several faults with variable throws and orientations (indicated by black and red arrows in Fig. 14a). Large-scale faults
485 mainly cross-cut the VCR orebody and underlying strata (indicated using yellow arrows, Fig. 14b). In contrast, several
486 small-scale faults and dykes cross-cut the entire stratigraphy (e.g., VCR and BLR orebodies, and the Transvaal
487 Supergroup rocks) as indicated by red arrows in Fig. 14c. Manzi et al. (2012b) spatially correlated the geological
488 structures (faults and dykes) defined by the 2003 legacy seismic data at the VCR mining level with groundwater
489 intersected through underground drilling data. The integrated data showed a good spatial correlation between water
490 and geological structures. Manzi et al. (2012b) hypothesized that the water found at the mining level originates from
491 the overlying near-surface fractured aquifer systems of the Transvaal Supergroup and travels through faults and dykes
492 to the mining levels. However, due to the low resolution of the large-offset 2003 legacy 3D seismic data in the near-
493 surface, the continuity of these faults and dykes into the overlying aquifer systems was never fully investigated (see
494 Fig. 14a-b). This study attempts to provide some seismic constraints on the near-surface geology and previous
495 interpretations using the SW analysis of the 2023 3D seismic data. Figure 14d shows the integration of 2003 depth-
496 converted pre-stack time migrated seismic data, pseudo-2D S-wave sections extracted from 2023 3D seismic data,
497 mine infrastructure (e.g., mining tunnel – MT), and mine geological structures (faults and dykes). Smoothing, by
498 increasing the gridding bin size, was applied to the presented S-wave section to suppress the more local variations
499 (i.e., subtle variations such as layering) and enhance the visibility of larger (regional) scale trends present in the S-
500 wave data. As stated already, Figure 14 shows that the P-wave seismic section lacks reflectivity in the near-surface
501 (top ~ 0.5 km); however, it exhibits strong reflectivity at deeper depths, i.e., between depth intervals of ~ 0.5 km to
502 3.5 km (Fig. 14a). Overlying the S-wave velocity model on the P-wave section enables near-surface variations and
503 structural complexity resolved by the S-wave velocity model, to be viewed with respect to deeper structures well
504 resolved by the P-wave seismic reflection method, including known water-bearing structures at the mining levels (Fig.
505 14c-d). The mine modelled and confirmed water-bearing geological structures at the mining levels include the three
506 north-south trending dykes (here referred to as D-1, D-2 and D-3) that cross-cut the gold orebodies (VCR and Upper
507 Elsburg Reef package) at depths between 3 and 3.5 km below the ground surface (Fig. 14d). The source of the water
508 found at the mining level, along these dykes, is unknown. Furthermore, the continuity of these structures above the
509 mining levels is not known since they are not well-defined on the current legacy seismic data. In determining the
510 linkage of these dykes with the overlying aquifers, we analysed the near-surface S-wave velocity zones and
511 investigated their spatial correlation with these dykes. The assumption is that, if the targeted structures intersect the
512 aquifers, then they have the potential to transport water from the overlying Chuniespoort Group dolomite aquifers to
513 the underground workings (Manzi et al., 2012b).

514 Figure 14d shows near-surface low-velocity zones (indicated by blue arrows, and with velocities varying from ~ 500
515 m/s to 4000 m/s) that may correspond to known major dykes (D-1, D-2, and D-3) and fault zones present in the vicinity
516 of the mine and confirmed by underground mapping and drilling. The locations of the low-velocity zones on the S-
517 wave section correlate well with the locations of the apparent fault zones and dykes imaged at the VCR mining level.
518 The S-wave low-velocity zones are possibly structurally weak zones (e.g., fault zones) that allowed for dyke
519 emplacement or are the weathered tops of the dykes. The dykes are mafic in composition and less competent in the

520 near-surface compared to silicate rocks, and therefore break down easily than the surrounding rocks, resulting in lower
 521 seismic velocities relative to the surrounding rocks (Evans et al., 1998). Noted on the seismic sections is that the
 522 reflector disturbances associated with these faults and/or dykes are not well-defined within the upper units of the
 523 Transvaal Supergroup (i.e., above the BLR orebody). This could be because (1), in the case of faults, their throws are
 524 not large enough to be resolved by the seismic data, and (2), in the case of the dykes, they are near-vertical with a
 525 thickness less than the resolution limit of the legacy seismic reflection data. These dykes and linked near-surface low-
 526 velocity zones are possible water source preferential flow-pathways that act as pathways for water migration from the
 527 Chuniespoort Group dolomites into the VCR and UER mining levels. Several similar dykes and faults that displace
 528 both the BLR and VCR orebodies in the area were detected through seismic attributes, and are reported by Manzi et
 529 al. (2012b).



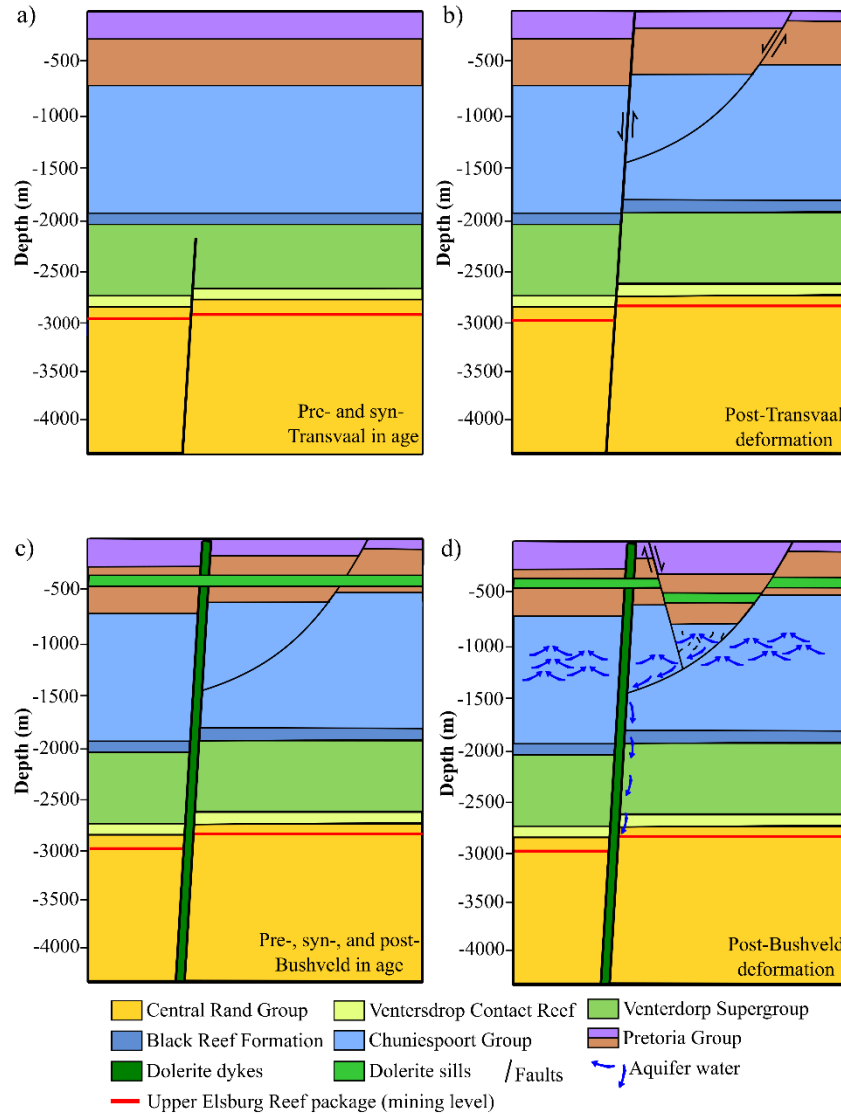
530
 531 **Figure 14: Integration of the P-wave reflection seismic data and S-wave velocity models. (a) Pre-stack time migrated seismic**
 532 **section (depth converted) extracted from the 2003 legacy 3D South Deep Gold Mine seismic data. The reflection seismic**
 533 **data show strong and continuous reflections related to the Black Reef (BLR) unconformity, and Ventersdorp Contact Reef**
 534 **(VCR) orebody, and the location of the mining tunnels (MT). The black arrows point to faults that displace the BLR and**
 535 **VCR unconformities. (b) P-wave reflection seismic sections with the near-surface S-wave velocity model and VCR dip**
 536 **attribute map. The yellow arrows point to large-scale faults displacing the VCR orebody. (c) P-wave reflection sections with**

537 the BLR dip-azimuth attribute map and VCR dip attribute map. The red arrows point to small-scale faults that seem to
538 cross-cut the entire stratigraphy. (d) Integrated 2003 depth-converted pre-stack time migrated seismic data, near-surface
539 S-wave velocity model, and mine geological structures (faults and dykes (D-1, D-2, and D-3)). The blue arrows indicate
540 surface zones that appear to exhibit potential linkages with the deep seismic reflection model and the geological structures
541 (faults and dykes) observed at the mining level and imaged by the legacy 2003 3D reflection seismic data.

543 5 Discussion

544 5.1 Subsurface conceptual geological model drawn from the integrated datasets

545 Overall, the S-wave velocity results attained in this study iterate the advantages and advances that can be made from
546 computing SW analysis on deep reflection seismic profiles. Comparing the geological information interpreted from
547 the S-wave velocity models with proximal borehole data and known geological characteristics of the area illustrates
548 that the subsurface information inferred from the S-wave velocity models is in agreement with a priori information.
549 In Figure 15, we provide a geological model and constrain the tectonic history of a portion of the Witwatersrand basin,
550 focusing on the deeper pre-Transvaal Supergroup and post-Bushveld tectonic events within the South Deep Gold
551 Mine. The geological model focuses on the combined near-surface and deeper P-wave reflection seismic, mine
552 mapping, and drilling information. The geological model commences with the deposition of the Central Rand Group
553 of the Witwatersrand Supergroup and the subsequent emplacement of the basaltic lavas of the Ventersdorp Supergroup
554 (Fig. 15a). This is followed by a pre-Transvaal deformation event that displaces the stratigraphy of both the Central
555 Rand Group and Ventersdorp Supergroup, respectively (Fig. 15a). Subsequently, the Chuniespoort and Pretoria
556 Groups of the Transvaal Supergroup are deposited (Fig. 15a). A post-Transvaal deformation event occurs thereafter,
557 reactivating pre-existing faults, forming faults that displace the entire stratigraphic sequence including the Transvaal
558 Supergroup and consists of associated splay faults (Fig. 15b). The faults act as planes of weaknesses and serve as a
559 pathway for preferential emplacement of intrusions (doleritic dykes) during pre-, syn-, and post-Bushveld event (Fig.
560 15c). Doleritic sills are emplaced at an angle to the doleritic dykes along bedding planes of the Pretoria Group rocks
561 (Fig. 15c). Lastly, slump faulting (post-Bushveld deformation) occurs due to the dissolution of dolomites of the
562 Chuniespoort Group and displaces the overlying Chuniespoort and Pretoria Group rocks (Fig. 15d).



563

564 **Figure 15: Generalized geological model illustrating the sequence of geological and deformation events identified within the**
 565 **study area: (a) deposition of the Central Rand Group and subsequent emplacement of the Venterdorp Supergroup,**
 566 **followed by a pre-Transvaal deformation event, and thereafter, the deposition of the Transvaal Supergroup (Chuniespoort**
 567 **and Pretoria Groups); (b) faulting associated with a post-Transvaal deformation event occurs reactivating pre-existing**
 568 **faults and displaces the entire stratigraphic sequence; (c) the intrusion of doleritic dykes and sills along planes of weaknesses**
 569 **such as faults and bedding planes (pre-, syn-, and post- Bushveld in age); (d) slump-faulting associated with the dissolution**
 570 **of dolomites results in the displacement of the overlying Chuniespoort and Pretoria Group rocks (post-Bushveld**
 571 **deformation). The dolomites of the Chuniespoort Group act as water sources (aquifers) and are displaced by faults and**
 572 **dykes that link them to the Upper Elsberg Reef package (underground workings at depth) and thus, act as pathways for**
 573 **water migration from the near-surface to underground workings (water preferential flow-pathways).**

574

575 **5.2 Delineating water preferential flow-pathways using shallow and deeper velocity models along with mine**
576 **mapping and drilling information**

577

578 Gold-bearing strata of the West Rand Goldfield are overlain by an approximately 1 km thick Chuniespoort Group
579 dolomite sequence, which is associated with karst systems that host considerable volumes of water (Fig. 15d,
580 Wolmarans, 1984; Van Niekerk and Van der Walt, 2006). The dolomitic aquifers are compartmentalized by several
581 fracture zones, fault zones, and dykes that link them to the underground workings and act as pathways of water
582 migration from the near-surface to underground workings (water preferential flow-pathways) (Fig. 15d, Manzi et al.,
583 2012b). Thus, water inflow in mining districts and water inrush are some of the serious and difficult-to-predict
584 challenges that affect mining processes and efficiency at the mine. Mining engineers have developed several ways of
585 reducing water inflow in mine workings, however, creating a reduction procedure is difficult without knowing the
586 exact locations of water pathways into the mining levels. In this study, we combine a near-surface S-wave velocity
587 model of the area, computed from the SW present in the high-resolution 2D and 3D seismic surveys, with legacy 3D
588 reflection seismic data, and information obtained from underground mine mapping and drilling to (1) characterize and
589 better understand near-surface lithological variations, and (2) enhance the imaging and delineation of faults and dykes
590 that extend from the near-surface to the deeper mining levels, which may act as water preferential flow-pathways (Fig.
591 15d). Generally, it is difficult to exactly determine which faults and dykes act as water preferential flow-pathways,
592 however the dykes integrated in this study have been confirmed through underground mapping to be water-bearing.
593 The results obtained in Figure 14 demonstrate that incorporating a near-surface S-wave velocity model along with
594 deeper P-wave seismic reflection models, mining level mapping, and drilling information enables a more
595 comprehensive, accurate, and reliable understanding of the subsurface environment to be drawn. In the case of South
596 Deep Gold Mine, it allowed for possible water preferential flow-pathways linking the Chuniespoort Group dolomites
597 with the deeper situated mining level to be delineated with more certainty. From the tectonic point of view, the near-
598 surface S-wave velocity models show that these dykes possibly cross-cut the entire stratigraphy including the
599 Transvaal Supergroup, indicating that these dykes were active post the deposition of the supergroup. The observation
600 indicates that these dykes are associated with pre-, syn-, and post-Bushveld deformation events and are likely
601 associated with intrusion events such as the Bushveld Complex, Pilanesberg Complex, and Umkondo Large Igneous
602 Province (Hartzer, 1989; Du Plessis and Walraven, 1990; Hartzer, 1995).

603

604 **6 Conclusion**

605 Surface wave analysis, conducted on DSR surveys using MASW, was used to investigate the near-surface (top 300
606 m) ~~inat~~ the vicinity of South Deep Gold Mine (South Africa) and investigate the effectiveness of integrating a near-
607 surface S-wave velocity model with a deep reflection seismic reflection data, mine mapping, and drilling information
608 to aid in delineating possible water preferential flow-pathways. To improve the robustness and spectral resolution of
609 the dispersion images and thus of the S-wave velocity imaging, we were compelled to use large spatial windows to

610 process the data. Additionally, to improve the data coverage and subsurface mapping in the study area, we utilize the
611 reciprocity principle to increase the data density in areas where no receiver locations, but source locations, were
612 present.

613 The attained near-surface S-wave velocity models revealed the occurrence of sheet-like layering, and the presence of
614 a S-wave velocity reversal zone, marking the contact between the Hekpoort and Timeball Hill Formations constituting
615 the upper formations in the study area, respectively. The S-wave velocity analysis also revealed the occurrence of
616 intrusive dykes, dip- and slump-faulting, which are all geological features characteristic of the West Rand Goldfield.
617 As the mine is to be extended in the near future, the near-surface results obtained in this research reveal the need for
618 more detailed near-surface investigations to be conducted to avoid placing future mining infrastructure in areas where
619 it may be compromised by prevalent geological features in the area, such as fractures, joints, and faults.

620 Integrating a near-surface velocity model with deeper P-wave seismic reflection data, mine mapping, and drilling
621 information introduces a novel approach to delineating possible water preferential flow-pathways to deep mining
622 levels and has proved to possess great potential for delineating water preferential flow-pathways and possible
623 structures that may pose a risk for deep mining. Of significance is that the results obtained in the study reveal that
624 there is value in conducting SW analysis on DSR exploration survey data. They show that complexities that cannot
625 be resolved by single techniques due to intrinsic limitations such as investigation depth, subsurface complexity, and
626 velocity inversion ambiguities can be better handled by integrating shallow and deep subsurface velocity models and
627 ground truth data.

628
629 Author Contributions. MSDM came up with the study idea, obtained funding, co-designed the seismic surveys, and
630 guided the manuscript preparation and write-up. LVS co-developed the manuscript concept, provided guidance on
631 data processing, and manuscript preparation. FKA designed the layered model used for surface wave processing,
632 processed the 2D surface wave profiles, and reviewed the manuscript. CC conducted the data preparation for
633 processing and provided valuable input in the data processing workflow. MK initiated the 3D processing and reviewed
634 the manuscript. JA assisted with the manuscript preparation (discussion write-up), and interpretation. SG carried out
635 the 3D processing, data integration, and manuscript writing. MSDM, LVS, and JB contributed significantly to the
636 overall data integration, interpretation, and processing.

637
638 Conflict of interest. The authors declare that they have no conflict of interest.

639
640 Acknowledgements. This research was funded by [the](#) FUTURE project (Fiber-optic sensing and UAV-platform
641 techniques for innovative mineral exploration) of the ERA-NET Cofound on Raw Materials (ERA-MIN3), Advanced
642 Orebody Knowledge (AOK), Vinnova (Sweden), Ministry of Universities and Research (Italy), National Agency for
643 Research (France), and DSI-NRF Centre of Excellence (CoE) for Integrated Mineral and Energy Resource Analysis

644 (CIMERA). Much gratitude goes to the Department of Science and Innovation (DSI) for funding the South African
645 partners in the [FUTURE project](#) ~~Future project~~. We would like to extend our gratitude to South Deep Gold Mine of
646 Gold Fields Ltd. for granting us access to their mine, permission to conduct research and publish the outcome of the
647 research. We also wish to extend our gratitude to [Smart Seismic Solutions \(S³\) for the acquisition of the 2023 2D and](#)
648 [3D reflection seismic surveys](#). ~~R~~researchers and postgraduate students from the Wits Seismic Research Centre at the
649 University of the Witwatersrand, Politecnico di Torino, Uppsala University, and Venda University [are also greatly](#)
650 [acknowledged](#) for their contributions to the success of the ERA-MIN3- ~~Future-FUTURE p~~Project.

651
652
653
654
655
656
657
658
659
660
661
662
663
664
665
666
667
668
669
670
671

673 **References**

- 674 Auken, E., and Christiansen, A.V.: Layered and laterally constrained 2D inversion of resistivity data. *Geophysics*,
675 69(3), 752-61, 2004.
- 676 Bekker, A., Planavsky, N., Rasmussen, B., Krapez, B., Hofmann, A., Slack, J., Rouxel, O., and Konhauser, K.: Iron
677 formations: Their origins and implications for ancient seawater chemistry. In *Treatise on geochemistry*
678 (Elsevier), 12, 561–628, 2014.
- 679 Boiero, D., and L.V. Socco.: Retrieving lateral variations from surface wave dispersion curve analysis: *Geophysical*
680 *Prospecting*, 58, 977-996, 2010.
- 681 Burger, A.J., and Coertze, F.J.: Radiometric age determinations on rocks from southern Africa up to the end of 1971.
682 *Bulletin Geological Society South Africa*, 58, 1-46, 1973.
- 683 Button, A., and Cawthorn, R.G.: Distribution of mafic sills in the Transvaal Supergroup, northeastern South
684 Africa. *Journal of the Geological Society*, 172(3), 357-367, 2015.
- 685 Campbell, G., and Crotty, J.H.: 3-D seismic mapping for mine planning purposes at the South Deep prospect. In:
686 Ross-Watt, D.A.J., Robinson, P.D.K. (Eds.), *Proceedings International Deep Mining Conference*. SAIMM
687 *Symposium Series*, S10, 2, 569–597, 1990.
- 688 Campbell, G., and Crotty, J.H.: The application of 3-D seismic surveys to mine planning. *South African Chamber of*
689 *Mines MINTEK*, Seminar, 1988.
- 690 Claerbout, J.F., and Green, I.: *Basic earth imaging*. Stanford University, Stanford, 2008.
- 691 Cousins, C.A.: The stratigraphy, structure and igneous rocks of the Transvaal System at the Western Areas Gold
692 Mine. *South African Journal of Geology*, 65(2), 13-40, 1962.
- 693 Coward, M.P., 1995. Structural and tectonic setting of the Permo-Triassic basins of northwest Europe. *Geological*
694 *Society, London, Special Publications*, 91(1), 7-39, 1995.
- 695 Dorland, H.C.: Provenance ages and timing of sedimentation of selected neoproterozoic and paleoproterozoic successions
696 on the Kaapvaal Craton. Unpublished Ph.D. thesis, Rand Afrikaans University, Johannesburg, South Africa,
697 326, 2004.
- 698 Du Plessis, C.P., and Walraven, F.: The tectonic setting of the Bushveld complex in Southern Africa, part 1: structural
699 deformation and distribution. *Tectonophysics*, 179 (3–4), 305–319, 1990.
- 700 Eaton, D.W., Milkereit, B., and Salisbury, M.H.: Hardrock seismic exploration. *Society of Exploration Geophysicists*,
701 1-6, 2003.

- 702 Eriksson, P.G., Schweitzer, J.K., Bosch, P.J.A., Schereiber, U.M., Van Deventer, J.L., and Hatton, C.J.: The Transvaal
703 sequence: an overview. *Journal of African Earth Sciences (and the Middle East)*, 16(1-2), 25-51, 1993b.
- 704 Evans, B.J., Urosevic, M., and Cocker, J.: The use of seismic methods for the detection of dykes, 1998.
- 705 Foti, S., Lai, C.G., and Lancellotta, R.: Porosity of fluid-saturated porous media from measured seismic wave
706 velocities. *Géotechnique*, 52(5), 359-373, 2002.
- 707 Franchi, F.: Petrographic and geochemical characterization of the Lower Transvaal Supergroup stromatolitic
708 dolostones (Kanye Basin, Botswana). *Precambrian Research*, 310, 93-113, 2018.
- 709 Frimmel, H.E., and Nwaila, G.T.: Geologic evidence of syngenetic gold in the Witwatersrand Goldfields, South
710 Africa, 2020.
- 711 Frimmel, H.E.: A giant Mesoarchean crustal gold-enrichment episode.: Possible causes and consequences for
712 exploration. In: Kelley, K., Golden, H.C (Eds.) *Building Exploration Capability for the 21st Century*. Society
713 of Economic Geologists, Special Publication, 209-234, 2014.
- 714 Frimmel, H.E.: The Witwatersrand Basin and Its Gold Deposits. In: Kröner, A., Hofmann, A. (eds) *The Archaean
715 Geology of the Kaapvaal Craton, Southern Africa*. Regional Geology Reviews. Springer, 2019.
- 716 Gibson, M.A.S.: Interpretation of the 2003 South Deep 3D seismic survey. Unpublished internal report to Gold Fields
717 Mining, 62, 2005.
- 718 Grandjean, G., and Bitri, A.: 2M-SASW: Multifold multichannel seismic inversion of local dispersion of Rayleigh
719 waves in laterally heterogeneous subsurfaces: application to the Super-Sauze earthflow, France. *Near Surface
720 Geophysics*, 4(6), 367-375, 2006.
- 721 Groves, P., Cascante, G., Dundas, D., and Chatterji, P.K.: Use of geophysical methods for soil profile
722 evaluation. *Canadian Geotechnical Journal*, 48(9), 1364-1377, 2011.
- 723 Graczyk, A., Malinowski M., and Bellefleur, G.: Enhancing 3D post-stack seismic data acquired in hardrock
724 environment using 2D curvelet transform. *Geophysical Prospecting* 63, 903–918, 2015.
- 725 Hartzer, F.J.: Stratigraphy, structure, and tectonic evolution of the crocodile river fragment. *South African Journal of
726 Geology*. 92 (2), 110–124, 1989.
- 727 Hartzer, F.J.: Transvaal Supergroup inliers: geology, tectonic development and relationship with the Bushveld
728 complex, South Africa. *Journal of African Earth Sciences*, 21 (4), 521–547, 1995.
- 729 Heinonen S., Kukkonen I., Heikkinen P., and Schmitt D.: High resolution reflection seismics integrated with deep
730 drill hole data in Outokumpu, Finland. *Geological Survey of Finland, Special Paper* 51, 105–118, 2011.

- 731 Katou, M., Abe, S., Saito H., and Sato, H.: Reciprocal data acquisition and subsequent waveform matching for
732 integrated onshore-offshore seismic profiling. *Geophysical Journal International*, 212, 509-521, 2017.
- 733 Khosro Anjom, F., Adler, F., and Socco, L.V.: Comparison of surface-wave techniques to estimate S-and P-wave
734 velocity models from active seismic data. *Solid Earth*, 15(3), 367-386, 2024.
- 735 Killick, A.M.: Pseudotachylites of the West Rand Goldfield, Witwatersrand Basin, South Africa, Doctor of Philosophy
736 Thesis, Rand Afrikaans University, Johannesburg South Africa. 18, 1992.
- 737 Knopoff, L., and Gangi, A. F.: Seismic reciprocity: *Geophysics*, 24, 681–691, 1959.
- 738 Kositcin, N., and Krapež, B.: Relationship between detrital zircon age-spectra and the tectonic evolution of the Late
739 Archaean Witwatersrand Basin, South Africa. *Precambrian Research*, 129(1-2), 141-168, 2004.
- 740 Laake, A., Strobbia, C., and Cutts, A.: Integrated approach to 3D near surface characterization in desert regions. first
741 break, 26(11), 2008.
- 742 Lin, C.P., Lin, C.H., and Chien, C.J.: Dispersion analysis of surface wave testing–SASW vs. MASW. *Journal of*
743 *Applied Geophysics*, 143, 223-230, 2017.
- 744 Malehmir, A., Koivisto, E., Manzi, M., Cheraghi, S., Durrheim, R.J., Bellefleur, G., Wijns, C., Hein, K.A., and King,
745 N.: A review of reflection seismic investigations in three major metallogenic regions: The Kevitsa Ni–Cu–
746 PGE district (Finland), Witwatersrand goldfields (South Africa), and the Bathurst Mining Camp
747 (Canada). *Ore Geology Reviews*, 56, 423-441, 2014.
- 748 Malehmir, A., Maries, G., Bäckström, E., Schön, M., and Marsden, P.: Developing cost-effective seismic mineral
749 exploration methods using a landstreamer and a drophammer. *Scientific Reports*, 7(1), 10325, 2017.
- 750 Malehmir, A., Wang, S., Lamminen, J., Brodic, B., Bastani, M., Vaittinen, K., Juhlin, C., and Place, J.: Delineating
751 structures controlling sandstone-hosted base-metal deposits using high-resolution multicomponent seismic
752 and radio-magnetotelluric methods: a case study from Northern Sweden. *Geophysical Prospecting*, 63(4),
753 774-797, 2015.
- 754 Manzi, M.S., Durrheim, R.J., Hein, K.A., and King, N.: 3D edge detection seismic attributes used to map potential
755 conduits for water and methane in deep gold mines in the Witwatersrand basin, South
756 Africa. *Geophysics*, 77(5), WC133-WC147, 2012a.
- 757 Manzi, M.S., Gibson, M.A., Hein, K.A., King, N., and Durrheim, R.J.: Application of 3D seismic techniques to
758 evaluate ore resources in the West Wits Line goldfield and portions of the West Rand goldfield, South
759 Africa. *Geophysics*, 77(5), WC163-WC171, 2012b.
- 760 Manzi, M.S., Hein, K.A., King, N., and Durrheim, R.J.: Neoarchaean tectonic history of the Witwatersrand Basin and
761 Ventersdorp Supergroup: New constraints from high-resolution 3D seismic reflection
762 data. *Tectonophysics*, 590, 94-105, 2013a.

- 763 Manzi, M.S., Hein, K.A.A., Durrheim, R., and King, N.: Seismic attribute analysis to enhance detection of thin gold-
764 bearing reefs: South Deep gold mine, Witwatersrand basin, South Africa. *Journal of Applied Geophysics*, 98,
765 212-228, 2013b.
- 766 Martin, D.M., Clendenin, C.W., Krapez, B., and McNaughton, N.J.: Tectonic and geochronological constraints on late
767 Archaean and Palaeoproterozoic stratigraphic correlation within and between the Kaapvaal and Pilbara
768 Cratons. *Journal of the Geological Society*, 155(2), 311-322, 1998.
- 769 Masethe, R.T., Manzi, M.S., and Durrheim, R.J.: Using legacy 3D seismic data and source parameters of mining-
770 induced earthquakes to mitigate the risk of rockbursting in Kloof Gold Mine, South Africa. *Geophysical*
771 *Prospecting*, 71(7 Special Issue: Mineral Exploration and Mining Geophysics), 1281-1311, 2023.
- 772 McCarthy, T.S.: The Witwatersrand Supergroup. *The Geology of South Africa*. Geological Society of South Africa,
773 2006.
- 774 Mutshafa, N., Manzi, M.S., Westgate, M., James, I., Brodic, B., Bourdeau, J.E., Durrheim, R.J., and Linzer, L.:
775 Seismic imaging of the gold deposit and geological structures through reprocessing of legacy seismic profiles
776 near Kloof–Driefontein Complex East Mine, South Africa. *Geophysical Prospecting*, 71(7 Special Issue:
777 Mineral Exploration and Mining Geophysics), 1181-1196, 2023.
- 778 Neduczka, B.: Stacking of surface waves. *Geophysics*, 72(2), V51-V58, 2007.
- 779 Nwaila, G.T., Frimmel, H.E., Zhang, S.E., Bourdeau, J.E., Tolmay, L.C., Durrheim, R.J., and Ghorbani, Y.: The
780 minerals industry in the era of digital transition: An energy-efficient and environmentally conscious
781 approach. *Resources Policy*, 78, 102851, (2022).
- 782 Nwaila, G.T., Ghorbani, Y., Becker, M., Frimmel, H.E., Petersen, J., and Zhang, S.: Geometallurgical approach for
783 implications of ore blending on cyanide leaching and adsorption behavior of Witwatersrand gold ores, South
784 Africa. *Natural Resources Research*, 29(2), 1007-1030, 2020a.
- 785 Osburn, K., Pretorius, H., Kock, D., King, N., Pillaye, R., and Hlangwane, M.: Enhanced geological modelling of the
786 Upper Elsburg reefs and VCR to optimize mechanized mine planning at South Deep Gold Mine. *Journal of*
787 *the Southern African Institute of Mining and Metallurgy*, 114(3), 265-273, 2014.
- 788 Papadopoulou, M., Da Col, F., Mi, B., Bäckström, E., Marsden, P., Brodic, B., Malehmir, A., and Socco, L.V.:
789 Surface-wave analysis for static corrections in mineral exploration: A case study from central
790 Sweden. *Geophysical Prospecting*, 68, 214-231, 2020.
- 791 Park, C.B., Miller, R.D., and Xia, J.: Imaging dispersion curves of surface waves on multi-channel record. In *Society*
792 *of Exploration Geophysicists technical program expanded abstracts 1998*, 1377-1380, 1998.
- 793 Parsons, C.F., and Killick, A.M.: A reassessment of the structure of the dolomite inliers southeast of Westonia. *South*
794 *African journal of geology*, 93(3), 438-442, 1990.

- 795 Pegah, E., and Liu, H.: Application of near-surface seismic refraction tomography and multichannel analysis of surface
796 waves for geotechnical site characterizations: A case study. *Engineering Geology*, 208, 100-113, 2016.
- 797 Pileggi, D., Rossi, D., Lunedei, E., and Albarello, D.: Seismic characterization of rigid sites in the ITACA database
798 by ambient vibration monitoring and geological surveys. *Bulletin of Earthquake Engineering*, 9, 1839-1854,
799 2011.
- 800 Pretorius, C.C., Jamison, A.A., and Irons, C.: Seismic exploration in the Witwatersrand Basin, Republic of South
801 Africa. In *Proceedings of Exploration '87*, ed. Garland, G.D. Ontario Geological Survey. 3, 241–253, 1989.
- 802 Rapetsoa, M.K., Manzi, M.S.D., Sihoyiya, M., Malehmir, A., James, I., Socco, L.V., Lepine, J., Colombero, C.,
803 Valeshin, O., and Durrheim, R.J.: Advanced seismic acquisition techniques in South African mines: Insights
804 from the FUTURE project. *Journal of the Southern African Institute of Mining and Metallurgy*, 125(1), 25-
805 32, 2025.
- 806 Saunders S., Lamb P., and Sweeney D.: High resolution seismic for resolving coal seam structure in difficult terrain.
807 *Geophysics* 22, 325–332, 1991.
- 808 Sheriff, R.E.: *Encyclopedic dictionary of applied geophysics*, 4th ed. Society of Exploration Geophysicists, Tulsa,
809 2002.
- 810 Smith, A.J., and Beukes, N.J.: Palaeoproterozoic Banded Iron formationhosted High-Grade Hematite Iron Ore
811 Deposits of the Transvaal Supergroup, South Africa. *Episodes*, 39(2), 269–284, 2016.
- 812 Socco L.V., Comina, C., and Khosro Anjom, F.: Time-average velocity estimation through surface-wave analysis:
813 Part 1 — S-wave velocity: *Geophysics*, 82(3), U49–U59, 2017.
- 814 Socco, L.V., and Strobbia, C.: Surface-wave method for near-surface characterization: A tutorial: *Near Surface*
815 *Geophysics*, 2, 165–185, 2004.
- 816 Socco, L.V., Boiero, D., Foti, S., and Wisén, R.: Laterally constrained inversion of ground roll from seismic reflection
817 records. *Geophysics*, 74(6), G35-G45, 2009.
- 818 Socco, L.V., Foti, S., and Boiero, D.: Surface-wave analysis for building near-surface velocity models—Established
819 approaches and new perspectives. *Geophysics*, 75(5), 75A83-75A102, 2010.
- 820 Socco, L.V., Papadopoulou, M., Federico, D.C., Chiara, C., Emma, B., Paul, M., and Alireza, M.: Surface wave
821 dispersion analysis in hard rock sites: challenges and opportunities. In *Geophysical Research Abstracts*, 21,
822 2019.
- 823 Strong, S.: Modelling complex near-surface features to improve shallow seismic exploration. *ASEG Extended*
824 *Abstracts*, 2018(1), 1-4, 2018.

- 825 Urosevic, M., Sherlock, D., Kepic, A., and Dodds, K.: 2007. Land seismic acquisition repeatability for time-lapse
826 monitoring of CO2 sequestration. ASEG Extended Abstracts, 2007(1), 1-1, 2007.
- 827 Van Niekerk, H.J., and Van der Walt, I.J.: Dewatering of the Far West Rand dolomitic area by gold mining activities
828 and subsequent ground instability. Land Degradation & Development, 17(4), 441-452, 2006.
- 829 Veevers, J.J.: Morphotectonics of rifted continental margins in embryo (East Africa), youth (Africa-Arabia), and
830 maturity (Australia). The Journal of Geology, 89(1), 57-82, 1981.
- 831 Vermaakt, D.T., Chunnet, I.E., and Anhaeusser, C.R.: Tectono-sedimentary processes which controlled the deposition
832 of the Ventersdorp Contact Reef within the West Wits Line. In Proceedings of the 15th Congress of the
833 Council for Mining and Metallurgical Institutions, South African Institute of Mining and Metallurgy, (3),
834 117-130, 1994.
- 835 Wilczynski, Z., Kaslilar, A., Malehmir, A., Manzi, M., Vivin, L., Lepine, J., Valishin, O., and Högdahl, K.: Ambient
836 noise surface-wave imaging in a hardrock environment: implications for mineral exploration. Geophysical
837 Journal International, 240(1), 571-590, 2025.
- 838 Wisén, R., and Christiansen, A.V.: Laterally and mutually constrained inversion of surface wave seismic data and
839 resistivity data. Journal of Environmental & Engineering Geophysics, 10(3), 251-262, 2005.
- 840 Wolmarans, J.F.: Ontwatering van die dolomietgebied aan die verre Wes-Rand: gebeure in perspektief. University of
841 Pretoria (South Africa), 1984.
- 842 Zhou, B., Hatherly, P., Peters, T., and Sun, W.: Experience with the issue of seismic surveying over basalts. ASEG
843 Extended Abstracts, 1-5, 2010.
- 844 Zhu, X., Valasek, P., Roy, B., Shaw, S., Howell, J., Whitney, S., Whitmore, N.D., and Anno, P.: Recent applications
845 of turning-ray tomography. Geophysics, 73(5), VE243-VE254, 2008.
- 846
- 847